Room-temperature-persistent magnetic interaction between coordination complexes and nanoparticles in maghemite-based nanohybrids

Leonardo Curti, Yoann Prado, Aude Michel, Delphine Talbot, Benoît Baptiste, Edwige Otero, Philippe Ohresser, Yves Journaux, Christophe Cartier Dit Moulin, Vincent Dupuis, et al.

Room-temperature-persistent magnetic interaction between coordination complexes and nanoparticles in maghemite-based nanohybrids.

Leonardo Curti, Yoann Prado, Aude Michel, Delphine Talbot, Benoît Baptiste, Edwige Otero, Philippe Ohresser, Yves Journaux, Christophe Cartier-dit-Moulin, Vincent Dupuis, Benoit Fleury, Philippe Sainctavit, Marie-Anne Arrio, Jérôme Fresnais* and Laurent Lisnard**

L. Curti, Y. Journaux, C. Cartier-dit-Moulin, B. Fleury, L. Lisnard

Sorbonne Université, CNRS, Institut Parisien de Chimie Moléculaire, IPCM, F-75005, Paris, France.

E-mail: laurent.lisnard@sorbonne-universite.fr

Y. Prado, A. Michel, D. Talbot, V. Dupuis, J. Fresnais

Sorbonne Université, CNRS, Laboratoire de Physicochimie des Électrolytes et Nanosystèmes interfaciaux, PHENIX, F-75005, Paris, France.

E-mail: Jerome.fresnais@sorbonne-universite.fr

B. Baptiste, P. Sainctavit, M.-A. Arrio

CNRS, Sorbonne Université, IRD, MNHN, Institut de Minéralogie, de Physique des Matériaux et de Cosmochimie, IMPMC, F-75005, Paris, France.

E-mail: marie-anne.arrio@sorbonne-universite.fr

E. Otero, P. Ohresser, P. Sainctavit

Synchrotron SOLEIL, L'Orme des Merisiers, Saint-Aubin, BP 48, 91192 Gif-sur-Yvette, France.

Keywords: maghemite, coordination complexes, hybrid nanoparticles, XAS, XMCD, magnetic interaction

Maghemite nanoparticles functionalized with Co(II) coordination complexes at their surface show a significant increase of their magnetic anisotropy. Magnetometric studies suggest an enhancement that is not related to surface disordering, and point to a molecular effect involving magnetic exchange interactions mediated by the oxygen atoms at the interface as its source. Field- and temperature-dependent X-ray absorption spectroscopy (XAS) and X-ray magnetic circular dichroism (XMCD) studies show that the magnetic anisotropy enhancement is not limited to surface atoms and involves the core of the nanoparticle. These studies also point to a mechanism driven by anisotropic exchange and confirm the strength of the magnetic exchange interactions. The coupling between the complex and the nanoparticle persists at room temperature. Simulations based on the XMCD data give an effective exchange field value through the oxido coordination bridge between the Co(II) complex and the nanoparticle that is comparable to the exchange field between iron ions in bulk maghemite. Further evidence of the effectiveness of the oxido coordination bridge in mediating the magnetic interaction at the interface is given with the Ni(II) analog to the Co(II) surface-functionalized nanoparticles. A substrate-induced magnetic response is observed for the Ni(II) complexes, up to room temperature.

1. Introduction

Early on, surface effects have been identified for the crucial yet intricate role they play in the magnetic properties of single-domain superparamagnetic nanoparticles,[1] whether the nanoparticles are metallic,[2–8] metal-oxide[9–13] or molecule-based.[14–16] The inherent presence at the surface of structural defects, disorder or strains can lead to a modified anisotropy for the spin carriers, and competitive exchange interactions between surface atoms or between the surface atoms and the inner ones can lead to canted, frustrated or disordered spins.[17–19] In the case of iron oxide nanoparticles, it has been well documented, with dedicated physical studies focused on the investigation of these phenomena.[20–27] And while chemical modifications of the surface were initially performed to help investigate surface effects,[28–32] surface functionalization has rapidly appeared as an efficient tool to modify the magnetic properties,[33,34] becoming all the more important considering the attractiveness of iron oxide-based nanoparticles for applications in biomedicine or data storage.[35–39] Ligand exchange has been a well-developed surface functionalization strategy,[40–43] so is metal ion chemisorption, and especially Co(II) ions, which have been widely used to functionalize maghemite.[30,34,44–52] In the case of Co(II) ions however, synthetic strategies focused on and resulted in aggregated, sometimes doped, samples. This led us to explore an alternative surface functionalization approach with a special emphasis on the use of soft aqueous conditions and the preparation of stable colloidal assemblies. It consists in the elaboration of hybrid materials where the anisotropic Co(II) complex [Co(TPMA)Cl_2] (TPMA: tris(2-pyridylmethyl)amine) is coordinated to the oxygen atoms at the surface of maghemite γ-Fe_2O_3 nanoparticles.[53] The thus surface-functionalized nanoparticles showed a significant increase of their coercive field and blocking temperature values associated to an enhanced anisotropy. Our preliminary study clearly indicated an enhanced behavior that could neither arise from each separated component nor be their sum, hinting at the existence of a magnetic interaction at the interface. Investigating the existence of such a magnetic interaction between the coordinated cobalt(II) complex and the iron ions at the nanoparticle surface, and identifying it as the source of the anisotropy enhancement is far from trivial and almost impossible with conventional spectroscopies or characterization techniques. However, X-ray absorption spectroscopy (XAS) and X-ray magnetic circular dichroism (XMCD) are the ideal local probe to differentiate and analyze the magnetic behavior of each metal ion, separately.

Indeed, XAS and XMCD are element-specific core-level spectroscopies that allow the determination of the local magnetic moment of the selected absorbing ion. In particular, investigating the $L_{2,3}$ edges of 3*d* metals which corresponds mostly to the electronic transition between a 2*p* core-level and an empty 3*d* level ($2p^6\ 3d^n$ to $2p^5\ 3d^{n+1}$) is equivalent to probing the magnetic orbitals of the 3*d* elements. We present here a XAS and XMCD study of the bare nanoparticles **γ-Fe_2O_3**, of the Co(II) and Ni(II) surface-functionalized nanoparticles, **γ-Fe_2O_3@{Co(TPMA)}**, and **γ-Fe_2O_3@{Ni(TPMA)}**, and of the parent pristine complexes, **[Co(TPMA)Cl_2]** and **[Ni(TPMA)Cl_2]**, and we demonstrate the existence of a strong magnetic interaction between the coordination complex and the nanoparticle that persists at room temperature. We postulate that the exchange interactions mediated by the oxido coordination bridges at the surface include anisotropic exchange to allow for the Co(II) ions to enhance the anisotropy of the nanoparticle. We also show that the exchange interactions promoted by the oxido coordination bridges are strong enough to yield a substrate-induced magnetic response in Ni(II) complexes when they are coordinated to the surface of the nanoparticles.

2. Results

Starting from size-sorted γ-Fe_2O_3 maghemite nanoparticles obtained via the Massart method,[54,55] we have prepared bare nanoparticles in basic media (**γ-Fe_2O_3**), electrostatically stabilized by tetramethylammonium cations, TMA^+, and functionalized them with the [Co(TPMA)Cl_2] complex (yielding **γ-Fe_2O_3@{Co(TPMA)}**) or its Ni(II) analog (to give **γ-Fe_2O_3@{Ni(TPMA)}**). The functionalization strategy, which we reported previously,[53] relies on the presence in basic media of negatively charged nucleophilic oxygen atoms at the surface of the particles, and in their accessibility in the absence of stabilizing capping ligands. It allows in soft conditions and aqueous media the coordination of metal ion complexes at the surface of the iron oxide nanoparticles thanks to the substitution of the chloride anions and the formation of oxido coordination bridges. DLS, TEM, and PXRD confirm that this surface functionalization method comes at no cost in size, with no structural changes, and maintain colloidal stability. Hydrodynamic diameters measured for the functionalized nanoparticles **γ-Fe_2O_3@{Co(TPMA)}** and **γ-Fe_2O_3@{Ni(TPMA)}**, 13.6 and 13.9, are similar to the Z_{ave} value measured for the bare objects **γ-Fe_2O_3**, 13.2 nm (see Figure S1 in the supporting information). Similarly, analysis of the TEM images indicates close size values ($\langle D \rangle$ = 5.9, 6.3, and 6.3 nm

for **γ-Fe_2O_3**, **γ-Fe_2O_3@{Co(TPMA)}** and **γ-Fe_2O_3@{Ni(TPMA)}** respectively, see Figures S2 to S4 in the supporting information). All the compounds show the $Fd\bar{3}m$ cubic structure of maghemite (see Figure S5 in the supporting information). Titration of the metal ions content indicates that in **γ-Fe_2O_3@{Co(TPMA)}** there are 66 {Co(TPMA)} complexes per nanoparticle, which corresponds to 0.53 complexes per nm^2 at the surface, and 1.36 % of the metallic content. Similar results are obtained for **γ-Fe_2O_3@{Ni(TPMA)}** and the functionalization with the Ni(II) complex (70 complexes per nanoparticle, 0.56 complexes/nm^2, 1.45 % of the metallic content), indicating comparable surface functionalization reaction yields for **γ-Fe_2O_3@{Co(TPMA)}** and **γ-Fe_2O_3@{Ni(TPMA)}** (77 and 82 %).

2.1. SQUID magnetometry

SQUID magnetic measurements on the frozen solutions of **γ-Fe_2O_3**, **γ-Fe_2O_3@{Co(TPMA)}** and **γ-Fe_2O_3@{Ni(TPMA)}** attest that the coordination of the Co(II) complex at the surface of the maghemite nanoparticles has the desired anisotropy enhancement effect. The measured coercive field, H_C, for **γ-Fe_2O_3@{Co(TPMA)}** is more than six times the value found for **γ-Fe_2O_3** (614 and 98 Oe respectively, ± 3kOe range shown in Figure 1). Consistently, the maximum of the zero-field-cooled (ZFC) magnetization curve for **γ-Fe_2O_3@{Co(TPMA)}** occurs at a significantly higher temperature than for **γ-Fe_2O_3** (from 17.7 K to 34.5 K, see Figure S8 in the supporting information) and the lognormal fit-determined blocking temperature,[56] $\langle T_B \rangle$, is also doubled (from 11.6 to 23.3 K). This gives an effective anisotropy constant (K_{eff} with $K_{eff} = 25k_B\langle T_B \rangle/\langle V \rangle$)[57,58] that increases from 37 kJ m^{-3} in **γ-Fe_2O_3** to 75 kJ m^{-3} in **γ-Fe_2O_3@{Co(TPMA)}**. On the other hand, in the case of **γ-Fe_2O_3@{Ni(TPMA)}**, no such enhancement is observed (H_C = 106 Oe, T_{max} = 18.5 K, $\langle T_B \rangle$ = 11.9 K and K_{eff} = 38 kJ m^{-3}). The two complexes should have the same reactivity, i.e. bind the same coordination sites and in a similar fashion. This supports the importance of the molecule nature in the anisotropy enhancement effect, as opposed to a functionalization method leading to an increase of the defects at the surface (whether they are structural defects or related to surface spins). Besides, saturation magnetization values are similar for **γ-Fe_2O_3@{Co(TPMA)}** and **γ-Fe_2O_3@{Ni(TPMA)}** (70 and 71 emu g^{-1}) and, actually, comparable to the value found for **γ-Fe_2O_3** (72 emu g^{-1}, see Figure S9 in the supporting information). No exchange bias has been detected in the hysteresis loops of **γ-Fe_2O_3@{Co(TPMA)}** and **γ-Fe_2O_3@{Ni(TPMA)}** measured after a field cooling (FC) procedure at 50 kOe (see Figure S11 in the supporting information), and the observed increase of the

H_C values in these FC loops is of the same order of magnitude in all the compounds (19% for **γ-Fe_2O_3**, 23% for **γ-Fe_2O_3@{Co(TPMA)}** and 16% for **γ-Fe_2O_3@{Ni(TPMA)}**). This would imply that the *initial* surface state of the nanoparticles is not altered by the functionalization method, which is sensible considering the small amount of complexes used (~ 70 for ca. 1245 Fe(III) ions at the surface, and ca. 4908 Fe(III) in total). The anisotropy enhancement observed in **γ-Fe_2O_3@{Co(TPMA)}** can thus not be explained by the formation of a frustrated spin-disordered shell, the increase of the existing surface spins disorder or by the modification of the surface spins canting. This further supports the molecular nature of the anisotropy enhancement effect, and points to the magnetic interactions between the coordination complex and the nanoparticle as its origin. Co(II) ions, where 1st order spin-orbit coupling occurs, will yield a strong anisotropic exchange with the Fe(III) ions of the nanoparticle surface. However, Ni(II) ions in an octahedral ligand field are weakly anisotropic, which, in the strong exchange limit, will yield minimal anisotropy transfer in **γ-Fe_2O_3@{Ni(TPMA)}**.

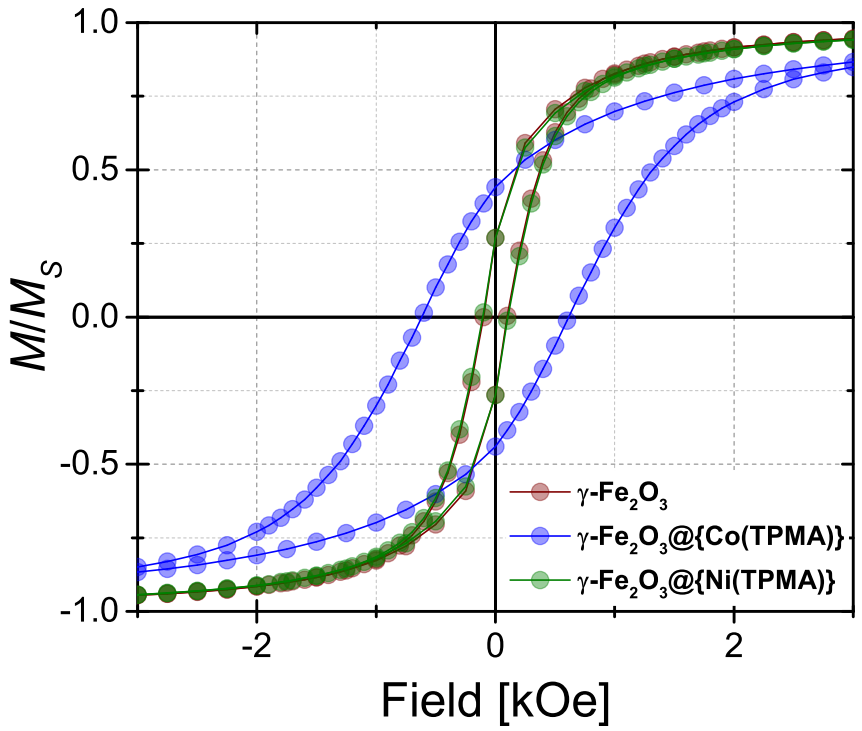

Figure 1. Magnetization v. field measurements for **γ-Fe_2O_3**, **γ-Fe_2O_3@{Co(TPMA)}** and **γ-Fe_2O_3@{Ni(TPMA)}** at 5 K. Saturation values have been normalized to 1 at 50 kOe.

2.2. XAS and XMCD

To further probe the magnetic properties, we have measured at various temperature and field values the XAS spectra and XMCD signals at the Fe, Co and Ni $L_{2,3}$ edges of **γ-Fe_2O_3**, **γ-Fe_2O_3@{Co(TPMA)}**, **γ-Fe_2O_3@{Ni(TPMA)}** and of the pristine complexes, **[Co(TPMA)Cl_2]**

and **[Ni(TPMA)Cl$_2$]** (see experimental methods for measurements details and sample preparation).

The XAS spectra at 4 K at the Fe $L_{2,3}$ edges for **γ-Fe$_2$O$_3$**, **γ-Fe$_2$O$_3$@{Co(TPMA)}** and **γ-Fe$_2$O$_3$@{Ni(TPMA)}** are all identical and typical of the Fe(III) ions in maghemite, and the XMCD signals show the distinct features associated with the two different types of environment found for the metal ions in the spinel structure (Figure 2 and Figure S16 in the supporting information).[24] Octahedral (*Oh*) Fe(III) ions show negative signals, which by convention indicate magnetic moments align parallel to the direction of the applied magnetic field, while the tetrahedral (*Td*) Fe(III) ions give positive signals, that is an alignment of its magnetic moment anti-parallel to the direction of the applied magnetic field. This reflects the anti-ferromagnetic interaction between *Oh* and *Td* Fe(III) ions. The XAS spectra of **γ-Fe$_2$O$_3$@{Co(TPMA)}** and **γ-Fe$_2$O$_3$@{Ni(TPMA)}** at 4 K and ± 60 kOe at the Co and Ni $L_{2,3}$ edges confirm the presence of octahedral +II metal ion complexes.[14,53] In comparison to the two pristine complexes, **[Co(TPMA)Cl$_2$]** and **[Ni(TPMA)Cl$_2$]**, the XAS spectra of **γ-Fe$_2$O$_3$@{Co(TPMA)}** and **γ-Fe$_2$O$_3$@{Ni(TPMA)}** at the Co and Ni L_3 edges feature changes that are consistent with surface coordination (see Figure S17-18 in the supporting information). In **γ-Fe$_2$O$_3$@{Co(TPMA)}**, the surface coordination —i.e. the substitution of the chloride anions by oxygen atoms from the surface— is accompanied by a clear modification of the ligand field strength.[53] The presence of a shoulder at 853.8 eV in the main Ni L_3 edge peak in **γ-Fe$_2$O$_3$@{Ni(TPMA)}** indicates a lower symmetry for the surface-coordinated Ni(II) complex.[14] It would result from the substitution of the chloride anions by surface oxygen atoms in a more constrained environment. The XMCD signals at the Co and Ni L_3 edges for **γ-Fe$_2$O$_3$@{Co(TPMA)}** and **γ-Fe$_2$O$_3$@{Ni(TPMA)}** are mainly negative, the magnetic moments for these ions align parallel to the direction of the field at 4 K and 60 kOe. The signal is less intense in **γ-Fe$_2$O$_3$@{Co(TPMA)}** than it is in its parent –non interacting– complex **[Co(TPMA)Cl$_2$]** (76 v. 95 % respectively). This lesser alignment with the direction of the field indicates the existence of competitive interactions at the surface and/or that the surface-coordinated complex is more anisotropic than its parent compound. The XMCD signal at the Ni L_3 edge is of comparable intensity in **γ-Fe$_2$O$_3$@{Ni(TPMA)}** and in **[Ni(TPMA)Cl$_2$]** (74 and 75 % respectively). There are no striking differences when comparing the shape of the XMCD signals at each metallic edge (see Figure S17-18 in the supporting information).

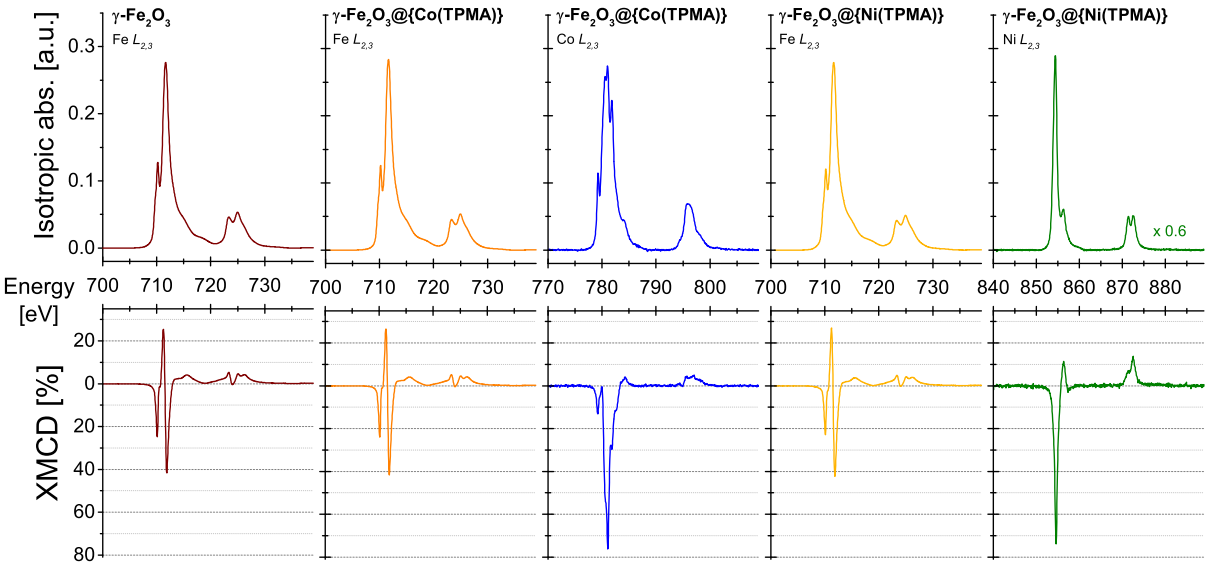

Figure 2. XAS spectra and XMCD signals at the Fe, Co and Ni $L_{2,3}$ edges measured at 4 K and ± 60 kOe for compounds **γ-Fe₂O₃**, **γ-Fe₂O₃@{Co(TPMA)}** and **γ-Fe₂O₃@{Ni(TPMA)}**. The XMCD signal is plotted as the percentage of the maximum intensity in the XAS spectrum.

2.2.1. Field-dependent XMCD

Knowing the energy values at which the XMCD signals at each edge and in each compound are the most intense, it is possible to measure the field-dependence of the XMCD signals. It is akin to perform element-specific magnetization curves and discriminate the magnetic behavior of each constituent metal ion.

At 4 K and between ± 60 kOe, the field-dependence of the XMCD signals of the *Oh* Fe(III) ions at the L_3 edge in **γ-Fe₂O₃**, **γ-Fe₂O₃@{Co(TPMA)}** and **γ-Fe₂O₃@{Ni(TPMA)}** all show an hysteretic behavior. As in the macroscopic SQUID measurements, a wider opening is observed in **γ-Fe₂O₃@{Co(TPMA)}** than in **γ-Fe₂O₃** or **γ-Fe₂O₃@{Ni(TPMA)}** which have similar openings (Figure 3). The determined H_C values at the *Oh* Fe(III) L_3 edge are 270 Oe (**1**), 590 Oe (**2**) and 230 Oe (**3**) (Table 1). This confirms the enhancement of the magnetic anisotropy when maghemite nanoparticles are functionalized by the Co(II) complex. Furthermore, the TEY detection mode we have used has a probing depth larger than the radii of the nanoparticles.[59] It implies that we probe the entire *Oh* Fe(III) content of the nanoparticle, meaning that the nanoparticle is almost entirely affected by the surface functionalization and shows an enhanced behavior. It does not just relate to the iron ions located at the surface and in close proximity to the coordinated Co(II) complexes. The field-dependence of the XMCD signal at the Co L_3 edge in **γ-Fe₂O₃@{Co(TPMA)}** also shows an opening of the hysteresis loop (H_C = 710 Oe) that is larger than in **γ-Fe₂O₃**, of the same order of magnitude than at the *Oh*

Fe L_3 edge (Table 1 and Figure 4), yet also larger. Actually, the different XMCD-detected H_C values observed at the Fe and Co L_3 edges in **γ-Fe_2O_3@{Co(TPMA)}** inform us about the influence the surface functionalization has on the whole nanoparticle. Taking the XMCD-detected H_C values in **γ-Fe_2O_3** at the Fe L_3 edge and in **γ-Fe_2O_3@{Co(TPMA)}** at the Co L_3 edge as the range from no to full Co(II) effect, the ratio with the ΔH_C value at the Fe L_3 edge between **γ-Fe_2O_3** and **γ-Fe_2O_3@{Co(TPMA)}** gives us an estimated 73 % of iron ions in the nanoparticle that are directly affected by the complexes (see supporting information for details). With surface iron ions amounting to 25 % of the total iron ions content, this clearly confirms the involvement of the Co(II) complexes in the anisotropy enhancement phenomenon in **γ-Fe_2O_3@{Co(TPMA)}**. Magnetic interactions that include a strong anisotropic exchange, such as the one coming from the existence of 1st order spin-orbit coupling in Co(II) octahedral ions, would allow the increase of the anisotropy of the Fe(III) surface ions.[60,61] The effect would then propagate into the core of the nanoparticle thanks to the existing exchange interactions between the *Oh* and *Td* Fe(III) ions. The overall magnetic behavior of the Co(II) ions is actually similar to that of the *Oh* Fe(III) ions, with rapid saturation and no sign inversion of the XMCD signal in the probed field range. This further shows that the functionalized nanoparticles behave homogeneously. The behavior of the Co(II) moment in **[Co(TPMA)Cl_2]** is markedly different, with no hysteresis loop opening at 4 K and a much slower saturation of the magnetization, indeed it is not reached at 60 kOe (Figure 4). All these observations support the existence of strong exchange interactions that the oxido coordination groups promote between the Co(II) ions of the surface-coordinated complex and the Fe(III) ions at the nanoparticle surface. Indeed, the magnetic interaction persists at 298 K and the field-dependence of the XMCD signals shows that the Co(II) and *Oh* Fe(III) magnetic moments in **γ-Fe_2O_3@{Co(TPMA)}** still behave identically (Figure 4 and Figure S19 in the supporting information). While no hysteresis opening is detected at the Co L_3 edge in **γ-Fe_2O_3@{Co(TPMA)}** at 298 K, the Co(II) magnetic moments still display a strong signal (near 50 % at 60 kOe) and saturate rapidly, when in the **[Co(TPMA)Cl_2]** complex, the signal is weak (less than 5 % at 60 kOe) with no sign of saturation. The field-dependence of the XMCD signal at the Ni L_3 edge in **γ-Fe_2O_3@{Ni(TPMA)}** shows that, as in **γ-Fe_2O_3@{Co(TPMA)}**, the magnetic behavior of the surface-coordinated complex is identical to that of the *Oh* Fe(III) ions w(Figure 4). At 4 K, the magnetization of the Ni(II) ions displays an hysteresis loop opening with a coercive field value close to that of the iron ions (H_C = 260 Oe), a rapid saturation and

homogeneous reversal. The magnetic interaction persists at 298 K. That the magnetic behavior of the Ni(II) ions shows such similarity to that of the *Oh* Fe(III) ions, is a further proof of the existence of strong exchange interactions mediated by the oxido coordination bridges at the nanoparticles surface. Given that *Oh* Ni(II) complexes do not possess strong anisotropy and show 2nd order spin-orbit coupling, the exchange interaction should be mainly isotropic. This striking magnetic behavior with both the opening of a hysteresis loop at the Ni L_3 edge at 4 K and a rapid saturation at 298 K is clearly induced by the maghemite. Incidentally, it also further confirms an anisotropy enhancement mechanism in **γ-Fe_2O_3@{Co(TPMA)}** driven by the existence and strength of the anisotropic exchange. Inversely, a strong isotropic exchange should suffice to make Ni(II) ions with a small anisotropy comparable to that of the Fe(III) surface ions follow the nanoparticle behavior.

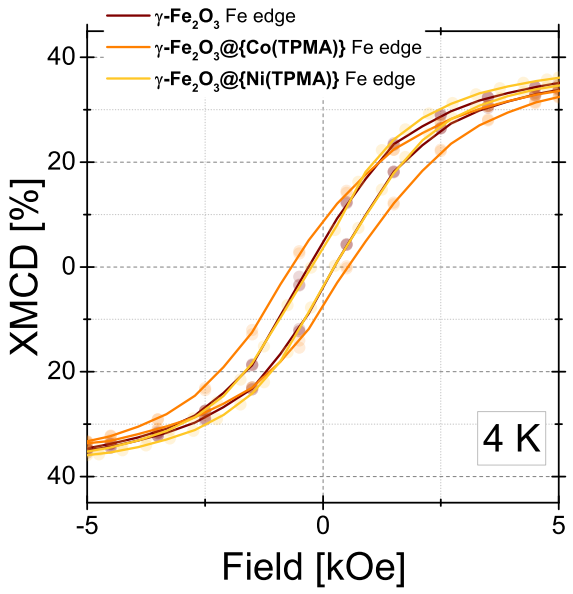

Figure 3. Field-dependence of the *Oh* Fe L_3 edge XMCD signals for **γ-Fe_2O_3**, **γ-Fe_2O_3@{Co(TPMA)}** and **γ-Fe_2O_3@{Ni(TPMA)}** at 4 K.

Table 1. Element-specific XMCD-detected coercive field values at 4 K for **γ-Fe_2O_3**, **γ-Fe_2O_3@{Co(TPMA)}** and **γ-Fe_2O_3@{Ni(TPMA)}**.

H_C values [Oe]	Fe L_3 edge	Co L_3 edge	Ni L_3 edge
γ-Fe_2O_3	270	/	/
γ-Fe_2O_3@{Co(TPMA)}	590	710	/
γ-Fe_2O_3@{Ni(TPMA)}	230	/	260

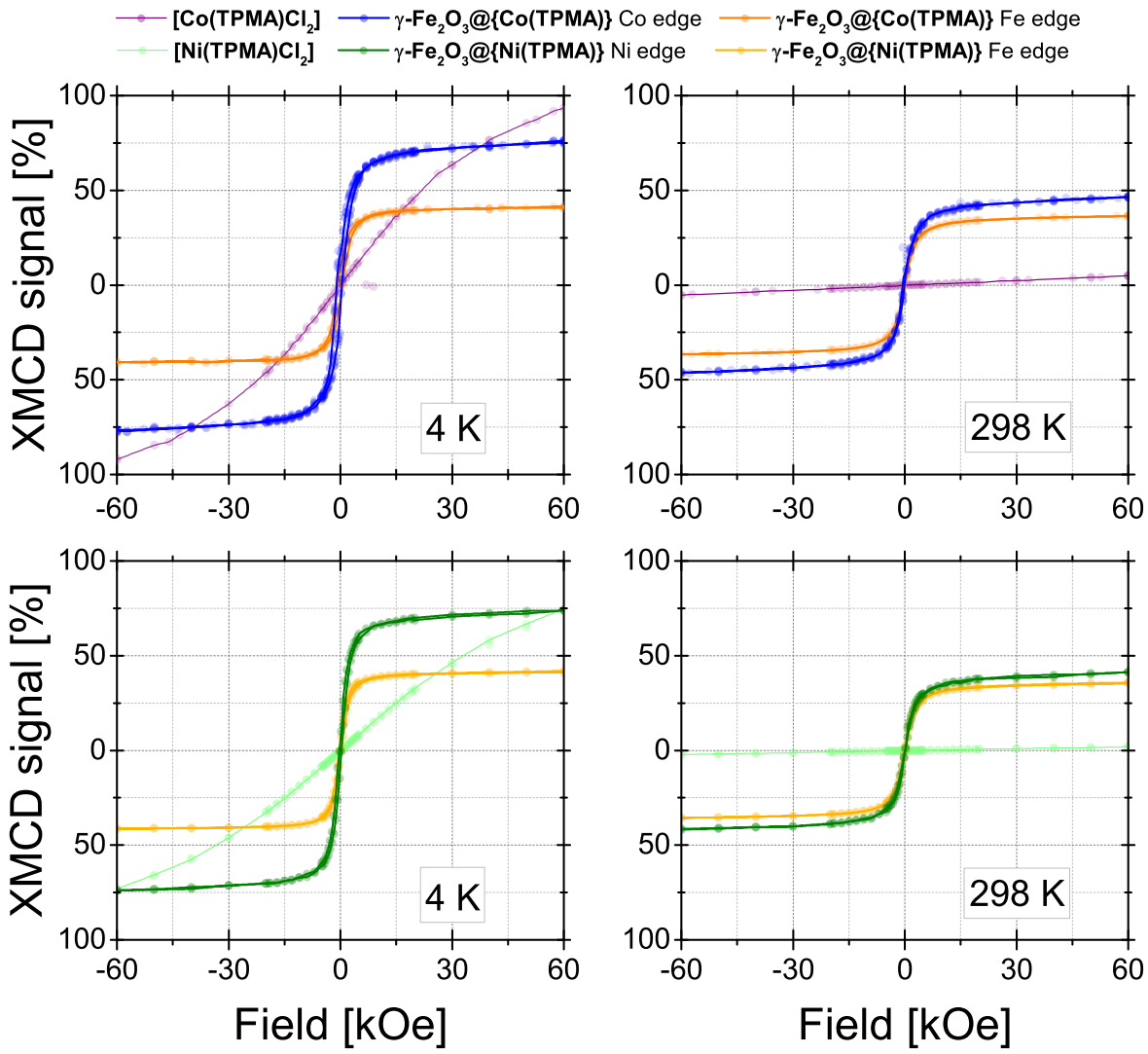

Figure 4. Field-dependence of the *Oh* Fe, Co and Ni L_3 edge XMCD signals for **γ-Fe₂O₃@{Co(TPMA)}**, **γ-Fe₂O₃@{Ni(TPMA)}**, **[Co(TPMA)Cl₂]** and **[Ni(TPMA)Cl₂]** at 4 K and 298 K.

Besides the advantageous influence that the Co(II) complex has on the anisotropy of the nanoparticle, our observations for both **γ-Fe₂O₃@{Co(TPMA)}** and **γ-Fe₂O₃@{Ni(TPMA)}** interestingly place the synthetic approach as a potentially viable method to achieve substrate-induced magnetic response at room temperature in a paramagnetic coordination complex, and via simple solution chemistry in soft conditions. It would complement the known, proven and yet harsher strategies, which have been developed on evaporated macrocyclic complexes deposited on metallic surfaces.[62–76] In the reported examples where paramagnetic coordination complexes are deposited on metal-oxide surfaces (CoO, Fe_3O_4), no substrate-induced magnetic responses were observed or measured for the grafted molecules at room temperature.[77–79]

2.2.2. Temperature-dependent XAS and XMCD

To further characterize the strength of the magnetic interaction between the coordination complex and the nanoparticle, we have measured the XAS spectra and XMCD signals at 100, 200 and 298 K and ± 60 kOe for all the compounds. At the Fe $L_{2,3}$ edges, there is almost no variation of the XAS spectra over the probed temperature range for **γ-Fe_2O_3**, **γ-Fe_2O_3@{Co(TPMA)}** and **γ-Fe_2O_3@{Ni(TPMA)}** (see Figures S19-21 in the supporting information). The shape of the XMCD signals does not change either, only their intensity does, with a small decrease when approaching room temperature (from 42 % to 36 % at the *Oh* Fe L_3 edge, see Figure S25 in the supporting information). This is expected, assuming that the intensity of the XMCD signal at the Fe edge will follow the temperature-dependence of the magnetization at saturation measured in **γ-Fe_2O_3**, **γ-Fe_2O_3@{Co(TPMA)}** and **γ-Fe_2O_3@{Ni(TPMA)}** (see Figure S10 in the supporting information). At the Co $L_{2,3}$ edges in compounds **γ-Fe_2O_3@{Co(TPMA)}** and **[Co(TPMA)Cl_2]**, the relative intensities of the two main features at 780.5 eV and 781 eV change with the temperature (see Figures S20 and S22 in the supporting information). This relates to the temperature dependence of the ligand field strength. At the Ni $L_{2,3}$ edges in compounds **γ-Fe_2O_3@{Ni(TPMA)}** and **[Ni(TPMA)Cl_2]**, no significant temperature-dependent changes in the XAS spectra have been observed (see Figures S21 and S23 in the supporting information). The temperature-dependence of the intensity of the XMCD signals at the Co and Ni L_3 edges in **γ-Fe_2O_3@{Co(TPMA)}** and **γ-Fe_2O_3@{Ni(TPMA)}** indicates that the strength of the interaction is similar in both systems (see Figure S25 in the supporting information). It shows a monotonous decrease between 4 and 298 K with a slightly higher slope between 100 and 298 K. And while these XMCD signal intensities remain high at room temperature (46 and 41 % of the XAS intensity for **γ-Fe_2O_3@{Co(TPMA)}** and **γ-Fe_2O_3@{Ni(TPMA)}** respectively), the decrease is of almost half the initial low temperature values. It is also more pronounced than that of the *Oh* Fe(III) ions. Nevertheless, when looking at the complexes, **[Co(TPMA)Cl_2]** and **[Ni(TPMA)Cl_2]**, the intensity of the signals drops abruptly above 4 K, down to 14 % and 5 % at 100 K, respectively. This suggests that the interaction between the complexes metal ions and the iron ions of the surface is of the same order of magnitude than the one between *Oh* and *Td* Fe(III) ions in the nanoparticle, albeit less intense.

Applying the magneto-optical sum rules[80–82] at the Co and Ni $L_{2,3}$ edges for compounds **γ-Fe_2O_3@{Co(TPMA)}**, **γ-Fe_2O_3@{Ni(TPMA)}**, **[Co(TPMA)Cl_2]** and **[Ni(TPMA)Cl_2]** gives the temperature-dependence of the magnetic moments (Figure 5). At 4 K, the calculated values for the moments of **[Co(TPMA)Cl_2]** and **[Ni(TPMA)Cl_2]** are below the SQUID determined ones (1.79 v. 2.20 μ_B and 1.58 v. 1.82 μ_B respectively, see Figure S12 in the supporting information), in line with the estimation of the magneto-optical sum rules error by Piamontenze *et al*.[83] The calculated moments values for Co(II) ions in **γ-Fe_2O_3@{Co(TPMA)}** and Ni(II) ions in **γ-Fe_2O_3@{Ni(TPMA)}** are, at 4 K, 1.54 and 1.46 μ_B, respectively. These values are below the one found in the pristine complexes, the magnetization of the surface-coordinated complexes along the direction of the applied field is lessened, particularly for the Co(II) complex. It indicates, as commented earlier with the intensity of the XMCD signals, the presence of competitive interactions at the surface as well as an increased local ion anisotropy. The values calculated for the moments at 298 K for **γ-Fe_2O_3@{Co(TPMA)}** and **γ-Fe_2O_3@{Ni(TPMA)}** (0.98 and 0.78 μ_B) further support the existence of strong exchange interactions between the surface-coordinated metal ion complexes and the Fe(III) ions of the nanoparticles. Indeed, for the paramagnetic complexes to reach such moment values at room temperature via magnetic dipolar interactions, magnetic fields values of 760 and 1120 kOe would need to be generated for **[Co(TPMA)Cl_2]** and **[Ni(TPMA)Cl_2]**, respectively (see Figure S13 in the supporting information).[62] The dipolar field generated by the nanoparticle at its surface amounts to 2.2 kOe only.

To estimate the strength of the interaction between the complexes and the nanoparticles, we have calculated the average exchange field (H_{ex}) that represents the result of all the possible interactions with both *Oh* and *Td* Fe(III) ions. The orbit, spin and total magnetic moments were calculated within the Ligand Field Multiplet theory with the Quanty code.[84–86] The eigenstates of Co(II) and Ni(II) were calculated using *Oh* symmetry and a fixed H_{ex} value, within an external 60 kOe magnetic field. A ligand field strength of 10*Dq* = 1 eV was used for both Co(II) and Ni(II). The magnetic moments (spin and orbit) were calculated at each temperature using the Boltzmann distribution. Adjusting the value of H_{ex} to simulate the shape of the temperature-dependence of the normalized XMCD-detected magnetic moments (see Figure 5), we can estimate H_{ex} values of 30 and 22 meV in **γ-Fe_2O_3@{Co(TPMA)}** and **γ-Fe_2O_3@{Ni(TPMA)}**, respectively. The interaction is stronger between the Co(II) complex and the nanoparticle than that between the Ni(II) complex and the nanoparticle. Actually, in

γ-Fe$_2$O$_3$@{Co(TPMA)}, the simulated exchange field value is quite comparable to the H_{ex} values calculated for the Fe(III) ions in the maghemite nanoparticles (30-40 meV, see Figure S26 in the supporting information). This highlights the efficacy of the coordinating surface oxygen atoms in promoting magnetic exchange.

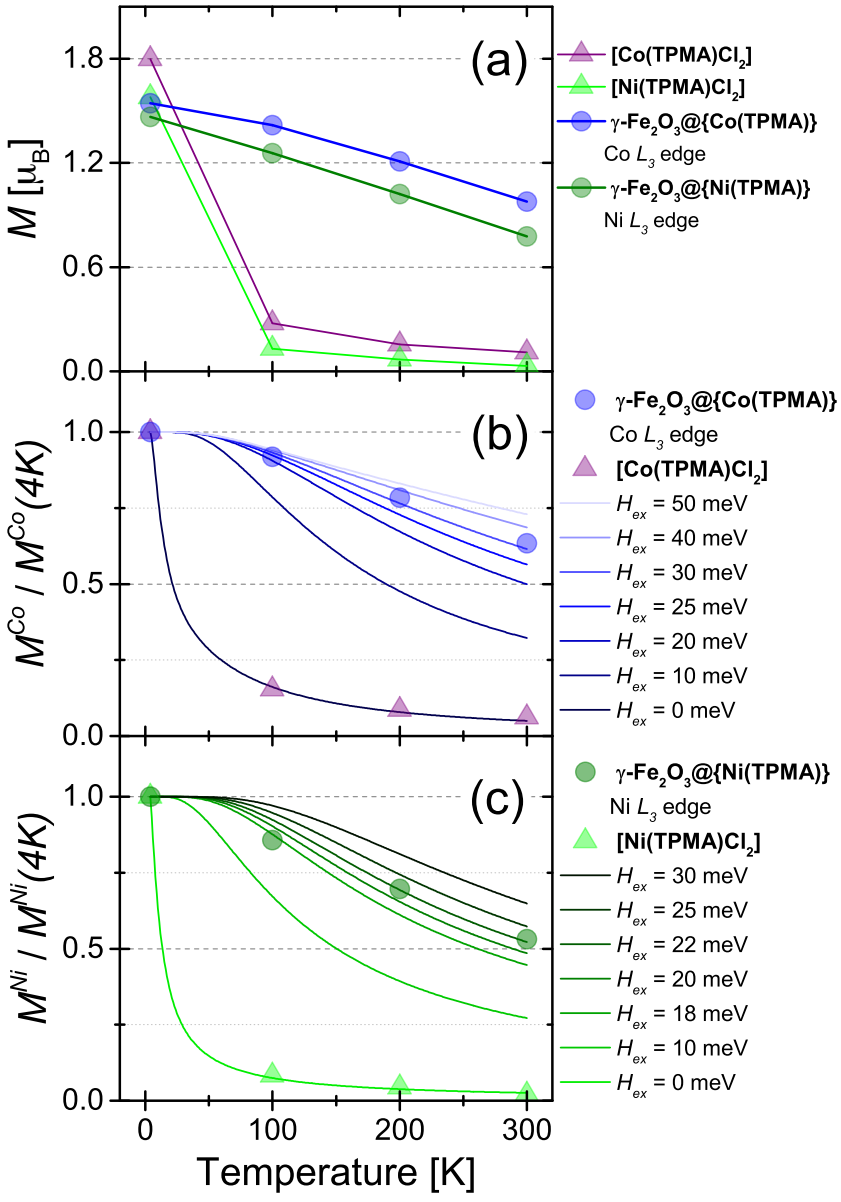

Figure 5. (a) Temperature-dependence of the Co(II) and Ni(II) magnetic moments determined by magneto-optical sum rules for **γ-Fe$_2$O$_3$@{Co(TPMA)}**, **γ-Fe$_2$O$_3$@{Ni(TPMA)}**, **[Co(TPMA)Cl$_2$]** and **[Ni(TPMA)Cl$_2$]**. (b) Simulation of *M(T)/M(4K)* for different exchange field values together with the normalized experimental Co(II) moment values for **γ-Fe$_2$O$_3$@{Co(TPMA)}** and **[Co(TPMA)Cl$_2$]**. (c) Simulation of *M(T)/M(4K)* for different exchange field values together with the normalized experimental Ni(II) moment values for **γ-Fe$_2$O$_3$@{Ni(TPMA)}** and **[Ni(TPMA)Cl$_2$]**.

3. Conclusion

We have shown that the use of readily available oxygen atoms at the surface of maghemite nanoparticles efficiently promotes magnetic exchange interactions with metal ion complexes via simple coordination bridges. Element-specific XAS and XMCD studies performed at various fields and temperatures indicate that the anisotropy enhancement of the Fe(III) ions of the nanoparticle by the Co(II) ions of the complexes is driven by anisotropic exchange, leading to higher magnetic anisotropy for the functionalized nanoparticles. Our study also demonstrates that the oxido-mediated exchange interactions persist at room temperature. Simulations of the temperature-dependent XMCD signals give an effective exchange field value between the coordination complex and the nanoparticle that is comparable in magnitude to the existing one between iron ions in the bulk of the maghemite ferrimagnet. That the on-surface magnetic interaction compares with the in-bulk one explains our observation when Ni(II) complexes are coordinated to the surface. We observe a substrate-induced magnetic response, even at room temperature.

At this stage, it is not possible to identify the exact nature of the interactions between the Co(II) ions and the Fe(III) ions (ferromagnetic or antiferromagnetic). Even if antiferromagnetic exchange interactions with either or both the *Oh* and *Td* Fe(III) ions are the sensible assumption, further surface functionalization strategies varying the magnetic and chemical nature of the complex are underway to entangle this specific issue by means of XAS and XMCD techniques. Nevertheless, our results highlight the role of the anisotropic exchange in the enhancement mechanism, as well as the viability of simple solution chemistry methods to efficiently couple magnetic molecules to metal oxide substrates.

4. Experimental methods

All reagents were used as purchased with no further purification.

Synthesis of the γ-Fe_2O_3 nanoparticles in acidic media. The solution was prepared according to literature procedures[54,55] ($\langle D \rangle$ = 5.85 nm, σ = 0.13, [Fe] = 1.14 M, %m = 7.58, %v = 0.154, pH = 1.8).

Coordination complexes. **[Co(TPMA)Cl_2]** and **[Ni(TPMA)Cl_2]** were prepared according to the literature procedure.[87] The corresponding metal ion hexahydrate chloride salt (0.34 mmol) dissolved in MeOH:DCM (1:4; 1 mL) is added to a DCM solution (1 mL) of the tris(2-

pyridylmethyl)amine) ligand (100 mg, 1eq.). After being stirred for one hour, the solution is filtered and layered with ethyl acetate. Crystals are obtained after a few days (yields: 56% for Co(II) and 96% for Ni(II)).

Preparation of the γ-Fe_2O_3 bare nanoparticles in basic media, stabilized with tetramethylammonium. Acidic γ-Fe_2O_3 nanoparticles (0.25 mL) are diluted with H_2O (0.75 mL) and MeOH (1.5 mL), and aqueous TMAOH (2.8 M, 0.5 mL) is brutally added to the solution under strong stirring. The solution is stirred for 4 hours at 60°C and left under stirring to cool to room temperature, leading to sample **γ-Fe_2O_3**. DLS gives Z_{ave} = 13.2 nm and TEM analysis gives $\langle D \rangle$ = 5.90 ± 1.8 nm (see Figures S1 and S2 in the supporting information). Precipitation of the nanoparticles for solid-state characterizations is achieved by the addition of acetone to the nanoparticles solution (three times the nanoparticle solution chosen volume). The suspension is placed on a NdFeB magnet in order to settle the particles and the supernatant is removed, yielding a paste-like solid that is used as such to prepare films (see below) or dried in a desiccator.

Preparation of the γ-Fe_2O_3 nanoparticles functionalized with [Co(TPMA)Cl_2]. **γ-Fe_2O_3@{Co(TPMA)}**. Acidic γ-Fe_2O_3 nanoparticles (0.25 mL) are diluted with H_2O (0.75 mL) and MeOH (1.5 mL). Then, aqueous TMAOH (2.8 M, 0.5 mL) is brutally added to the solution under strong stirring, followed by the addition of a fresh [Co(TPMA)Cl_2] solution in MeOH (10 mM, 0.5 mL) and of H_2O (0.5 mL). The solution is stirred for 4 hours at 60°C and left under stirring to cool to room temperature, leading to **γ-Fe_2O_3@{Co(TPMA)}**. DLS gives Z_{ave} = 13.6 nm and TEM analysis gives $\langle D \rangle$ = 6.33 ± 1.4 nm (see Figures S1 and S3 in the supporting information). Precipitation of the nanoparticles for solid-state characterizations is achieved as described for **γ-Fe_2O_3**.

Preparation of the γ-Fe_2O_3 nanoparticles functionalized with [Ni(TPMA)Cl_2]. **γ-Fe_2O_3@{Ni(TPMA)}**. Acidic γ-Fe_2O_3 nanoparticles (0.25 mL) are diluted with H_2O (0.75 mL) and MeOH (1.5 mL). Then, aqueous TMAOH (2.8 M, 0.5 mL) is brutally added to the solution under strong stirring, followed by the addition of a fresh [Ni(TPMA)Cl_2] solution in MeOH (10 mM, 0.5 mL) and of H_2O (0.5 mL). The solution is stirred for 4 hours at 60°C and left under stirring to cool to room temperature, leading to **γ-Fe_2O_3@{Ni(TPMA)}**. DLS gives Z_{ave} = 13.9 nm and TEM analysis gives $\langle D \rangle$ = 6.29 ± 1.6 nm (see Figures S1 and S4 in the supporting

information). Precipitation of the nanoparticles for solid-state characterizations is achieved as descried for **γ-Fe_2O_3**.

Dynamic light scattering (DLS). DLS measurements were performed on a MALVERN NanoZS (Malvern Instruments) at λ = 632 nm and backscattering detection mode (θ = 173°) using disposable plastic cells at room temperature. Before each measurement the sample was equilibrated for 60 seconds. For each sample, we have performed 3 consecutive measurements and, in each measurement, the scattered light was collected during 10 runs (each with a duration of 6 seconds) at a fixed position (4.65 cm). Material parameters: refractive index (RI) = 3; absorption = 0.5. Dispersant parameters (MeOH-H_2O 50:50 v/v): temperature = 25 °C; viscosity = 1.8027 cP; RI = 1.343.

Transmission electron microscopy (TEM). Images have been performed on a JEOL 100CX2 microscope with 65 keV incident electrons focused on the specimen.

Inductively coupled plasma atomic emission spectroscopy (ICP-AES). The total iron, cobalt and nickel concentrations were determined by ICP-AES on a Thermo Scientific™ iCAP™ 6200 spectrometer equipped with a Cetac ASX-520 autosampler spectrometer AAS after degrading the precipitated particles in HCl (37%).

Powder X-ray diffraction. Patterns were collected on a X'Pert Pro MPD Panalytical diffractometer in Bragg-Brentano geometry equipped with a Co−K**α** radiation source ($\lambda_{K\alpha1}$ = 1.78901 Å, $\lambda_{K\alpha2}$ = 1.79290 Å) and an X'Celerator detector. The paste-like solid forms of **γ-Fe_2O_3**, **γ-Fe_2O_3@{Co(TPMA)}** and **γ-Fe_2O_3@{Ni(TPMA)}** were suspended in MeOH and drop-casted on the silicon wafer sample holder, and dried in air prior to data collection.

SQUID Magnetic measurements. Magnetic measurements on frozen solutions of the as-prepared nanoparticles solutions were carried out with a Quantum Design MPMS-XL magnetometer working in dc mode. The solution (0.1 mL) is placed in a 0.2 mL eppendorf and inserted in the cryostat of the SQUID magnetometer and frozen directly from room temperature to 100K in zero magnetic field. ZFC/FC measurements were performed at 50 Oe with a 2 K min^{-1} sweeping rate. Hysteresis curves were measured at 5 K and ± 50 kOe. Field-cooled hysteresis loops were measured after cooling the samples from 250 K to 5 K under a 50 kOe applied magnetic field. Magnetic measurements on solid samples were carried out with a Quantum Design MPMS3 magnetometer in dc mode. The dried precipitated nanoparticles were restrained in a capsule. Solid-state samples were used to measure first magnetisation curves at 5 K between 0 and 50 kOe, determine saturation magnetization

values, and measure the temperature-dependence of the saturation magnetization between 5 and 300 K at 50 kOe.

XAS and XMCD measurements. XAS spectra and XMCD signals at the Fe, Co and Ni $L_{2,3}$ edges were measured on the soft X-ray beamline DEIMOS[88] at synchrotron SOLEIL (France). Circularly polarized photons delivered by an Apple II undulator are monochromatized by a VGD grating monochromator working in the inverse Petersen geometry. All reported spectra were measured using total electron yield (TEY) detection under a 10^{-10} mbar UHV. The XMCD signals were recorded by both flipping the circular polarization (either left or right helicity) and the applied magnetic field (either +60 kOe or -60 kOe). The XMCD signal is obtained as the difference $\sigma_{XMCD} = \sigma^- - \sigma^+$ where $\sigma^- = [\sigma_L(H^-) + \sigma_R(H^+)]/2$, $\sigma^+ = [\sigma_L(H^+) + \sigma_R(H^-)]/2$, σ_L (σ_R) is the cross-section with left (right) polarised X-rays, and H^+ (H^-) the magnetic field parallel (antiparallel) to the X-ray propagation vector. This procedure ensured a high signal-to-noise ratio and allowed us to discard any spurious systematic signals. The XMCD-detected magnetization curves are the field dependence of the dichroic signal. The XMCD amplitude is measured at the energy of its maximum amplitude (711.86 eV for Oh Fe in **γ-Fe_2O_3**, **γ-Fe_2O_3@{Co(TPMA)}** and **γ-Fe_2O_3@{Ni(TPMA)}**, 781.06 eV for Co in **γ-Fe_2O_3@{Co(TPMA)}**, 781.01 eV for Co in **[Co(TPMA)Cl_2]**, and 854.06 eV for Ni in **γ-Fe_2O_3@{Ni(TPMA)}** and **[Ni(TPMA)Cl_2]**) by quickly switching the circular polarisation thanks to the EMPHU undulator[88] available on DEIMOS beamline. Measurements for **γ-Fe_2O_3**, **γ-Fe_2O_3@{Co(TPMA)}** and **γ-Fe_2O_3@{Ni(TPMA)}** were obtained on samples prepared as follows: a freshly precipitated, un-dried nanoparticle paste-like solid obtained from 100 μL of the synthesis solution is further washed with acetone and sonicated. The suspension is placed on a NdFeB magnet in order to settle the particles and the supernatant is removed. The solid is then suspended in MeOH (50 μL), and drop-casted (5-7 μL) on a silicon wafer ((100), N-As, 9.5x5x0.275 mm) that is left to dry in air, forming homogeneous micrometric film. The wafers for **[Co(TPMA)Cl_2]** and **[Ni(TPMA)Cl_2]** are obtained by drop-casting 5 mM DCM solutions of the complexes. Samples **γ-Fe_2O_3**, **γ-Fe_2O_3@{Co(TPMA)}** and **γ-Fe_2O_3@{Ni(TPMA)}** were measured with 0° incident angle between the X-ray propagation vector and the substrate normal. A 54° incident angle was used to collect data at 4 K for **[Co(TPMA)Cl_2]** and **[Ni(TPMA)Cl_2]**. The background in the Fe edges spectra of **γ-Fe_2O_3**, **γ-Fe_2O_3@{Co(TPMA)}** and **γ-Fe_2O_3@{Ni(TPMA)}**, in **[Co(TPMA)Cl_2]** and in **[Ni(TPMA)Cl_2]** were corrected using arctangents functions to fit the $2p_{3/2}$ and $2p_{1/2}$ to continuum absorption steps.[89] The XAS spectra and XMCD signals at the

Co and Ni edges in **γ-Fe_2O_3@{Co(TPMA)}** and **γ-Fe_2O_3@{Ni(TPMA)}** were corrected by subtracting the experimental backgrounds obtained by measuring the XAS and XMCD at the Co and Ni $L_{2,3}$ edge in **γ-Fe_2O_3**. The areas of the spectra were then normalized to one. Supporting information Figures S13-14 give a graphical representation of the steps used.

Acknowledgements

This work was supported by the Centre National de la Recherche Scientifique (CNRS, France), the Ministère de l'Enseignement Supérieur et de la Recherche (MESR, France) and by the LabEx MiChem part of French state funds managed by the ANR within the Investissements d'Avenir programme under reference ANR-11-IDEX-0004-02. We acknowledge SOLEIL for provision of synchrotron radiation facilities (Proposals 20151305 and 20170454). Elemental analysis was supported by the IPGP multidisciplinary program PARI, and by Paris–IdF region SESAME Grant no. 12015908. We thank the staff of the low temperature physical measurement MPBT technical platform in Sorbonne Université.

References

[1] J. M. D. Coey, *Phys. Rev. Lett.* **1971**, *27*, 1140.
[2] T. Furubayashi, I. Nakatani, N. Saegusa, *J. Phys. Soc. Jpn.* **1987**, *56*, 1855.
[3] I. M. L. Billas, A. Châtelain, W. A. de Heer, *Science* **1994**, *265*, 1682.
[4] F. Bødker, S. Mørup, S. Linderoth, *Phys. Rev. Lett.* **1994**, *72*, 282.
[5] J. P. Chen, C. M. Sorensen, K. J. Klabunde, G. C. Hadjipanayis, *Phys. Rev. B* **1995**, *51*, 11527.
[6] A. Hernando, E. Navarro, M. Multigner, A. R. Yavari, D. Fiorani, M. Rosenberg, G. Filoti, R. Caciuffo, *Phys. Rev. B* **1998**, *58*, 5181.
[7] M. Respaud, J. M. Broto, H. Rakoto, A. R. Fert, L. Thomas, B. Barbara, M. Verelst, E. Snoeck, P. Lecante, A. Mosset, J. Osuna, T. O. Ely, C. Amiens, B. Chaudret, *Phys. Rev. B* **1998**, *57*, 2925.
[8] K. W. Edmonds, C. Binns, S. H. Baker, S. C. Thornton, C. Norris, J. B. Goedkoop, M. Finazzi, N. B. Brookes, *Phys. Rev. B* **1999**, *60*, 472.
[9] A. E. Berkowitz, J. A. Lahut, I. S. Jacobs, L. M. Levinson, D. W. Forester, *Phys. Rev. Lett.* **1975**, *34*, 594.
[10] A. H. Morrish, K. Haneda, P. J. Schurer, *J. Phys. Colloques* **1976**, *37*, C6.
[11] K. Haneda, H. Kojima, A. H. Morrish, P. J. Picone, K. Wakai, *Journal of Applied Physics* **1982**, *53*, 2686.
[12] A. H. Morrish, K. Haneda, *Journal of Magnetism and Magnetic Materials* **1983**, *35*, 105.
[13] S. Linderoth, P. V. Hendriksen, F. Bo/dker, S. Wells, K. Davies, S. W. Charles, S. Mo/rup, *Journal of Applied Physics* **1994**, *75*, 6583.
[14] Y. Prado, M.-A. Arrio, F. Volatron, E. Otero, C. Cartier dit Moulin, P. Sainctavit, L. Catala, T. Mallah, *Chem. - Eur. J.* **2013**, 6685.
[15] Y. Prado, S. Mazerat, E. Rivière, G. Rogez, A. Gloter, O. Stéphan, L. Catala, T. Mallah, *Adv. Funct. Mater.* **2014**, *24*, 5402.
[16] L. Zhang, M.-A. Arrio, S. Mazerat, L. Catala, W. Li, E. Otero, P. Ohresser, L. Lisnard, C. Cartier dit Moulin, T. Mallah, P. Sainctavit, *Inorg. Chem.* **2021**, *60*, 16388.

[17] A. E. Berkowitz, R. H. Kodama, S. A. Makhlouf, F. T. Parker, F. E. Spada, E. J. McNiff, S. Foner, *Journal of Magnetism and Magnetic Materials* **1999**, *196*, 591.
[18] X. Batlle, A. Labarta, *J. Phys. D-Appl. Phys.* **2002**, *35*, R15.
[19] D. Fiorani, Ed. , *Surface Effects in Magnetic Nanoparticles*, Spinger US, **2005**.
[20] F. T. Parker, M. W. Foster, D. T. Margulies, A. E. Berkowitz, *Phys. Rev. B* **1993**, *47*, 7885.
[21] J. L. Dormann, F. D'Orazio, F. Lucari, E. Tronc, P. Prené, J. P. Jolivet, D. Fiorani, R. Cherkaoui, M. Noguès, *Phys. Rev. B* **1996**, *53*, 14291.
[22] F. Gazeau, J. C. Bacri, F. Gendron, R. Perzynski, Yu. L. Raikher, V. I. Stepanov, E. Dubois, *Journal of Magnetism and Magnetic Materials* **1998**, *186*, 175.
[23] E. Tronc, A. Ezzir, R. Cherkaoui, C. Chanéac, M. Noguès, H. Kachkachi, D. Fiorani, A. M. Testa, J. M. Grenèche, J. P. Jolivet, *Journal of Magnetism and Magnetic Materials* **2000**, *221*, 63.
[24] S. Brice-Profeta, M.-A. Arrio, E. Tronc, N. Menguy, I. Letard, C. Cartier dit Moulin, M. Noguès, C. Chanéac, J.-P. Jolivet, Ph. Sainctavit, *Journal of Magnetism and Magnetic Materials* **2005**, *288*, 354.
[25] G. Rosa, H. Guerrero, D. Levy, A. Álvarez-Herrero, R. P. del Real, *Journal of Applied Physics* **2005**, *97*, 064314.
[26] Y. Komorida, M. Mito, H. Deguchi, S. Takagi, A. Millan, N. J. O. Silva, F. Palacio, *Appl. Phys. Lett.* **2009**, *94*, 202503.
[27] T. J. Daou, J.-M. Greneche, S.-J. Lee, S. Lee, C. Lefevre, S. Bégin-Colin, G. Pourroy, *J. Phys. Chem. C* **2010**, *114*, 8794.
[28] A. M. van der Kraan, *physica status solidi (a)* **1973**, *18*, 215.
[29] F. Itoh, M. Satou, *Jpn. J. Appl. Phys.* **1975**, *14*, 2091.
[30] Y. Tokuoka, S. Umeki, Y. Imaoka, *J. Phys. Colloques* **1977**, *38*, C1.
[31] S. Mørup, *Journal of Magnetism and Magnetic Materials* **1983**, *39*, 45.
[32] Y. Fukumoto, K. Matsumoto, Y. Matsui, *Journal of Applied Physics* **1991**, *69*, 4469.
[33] F. E. Spada, A. E. Berkowitz, N. T. Prokey, *Journal of Applied Physics* **1991**, *69*, 4475.
[34] F. E. Spada, F. T. Parker, A. E. Berkowitz, T. J. Cox, *Journal of Applied Physics* **1994**, *75*, 5562.
[35] Q. Dai, D. Berman, K. Virwani, J. Frommer, P.-O. Jubert, M. Lam, T. Topuria, W. Imaino, A. Nelson, *Nano Lett.* **2010**, *10*, 3216.
[36] N. Lee, D. Yoo, D. Ling, M. H. Cho, T. Hyeon, J. Cheon, *Chem. Rev.* **2015**, *115*, 10637.
[37] L. Gloag, M. Mehdipour, D. Chen, R. D. Tilley, J. J. Gooding, *Adv. Mater.* **2019**, *0*, 1904385.
[38] S. Furrer, P. Ebermann, M. A. Lantz, H. Rothuizen, W. Haeberle, G. Cherubini, R. D. Cideciyan, S. Tsujimoto, Y. Sawayashiki, N. Imaoka, Y. Murata, T. Ueyama, Y. Akano, T. Kaneko, H. Suzuki, M. Shirata, K. Naoi, T. Koike, H. Doshita, *IEEE Transactions on Magnetics* **2021**, *57*, 1.
[39] Z. Ma, J. Mohapatra, K. Wei, J. P. Liu, S. Sun, *Chem. Rev.* **2021**, DOI 10.1021/acs.chemrev.1c00860.
[40] C. R. Vestal, Z. J. Zhang, *J. Am. Chem. Soc.* **2003**, *125*, 9828.
[41] T. J. Daou, J. M. Grenèche, G. Pourroy, S. Buathong, A. Derory, C. Ulhaq-Bouillet, B. Donnio, D. Guillon, S. Begin-Colin, *Chem. Mater.* **2008**, *20*, 5869.
[42] A. Glaria, M. L. Kahn, A. Falqui, P. Lecante, V. Collière, M. Respaud, B. Chaudret, *ChemPhysChem* **2008**, *9*, 2035.
[43] D. Peddis, F. Orrù, A. Ardu, C. Cannas, A. Musinu, G. Piccaluga, *Chem. Mater.* **2012**, *24*, 1062.
[44] S. Umeki, S. Saitoh, Y. Imaoka, *IEEE Transactions on Magnetics* **1974**, *10*, 655.
[45] Y. Imaoka, S. Umeki, Y. Kubota, Y. Tokuoka, *IEEE Transactions on Magnetics* **1978**, *14*, 649.
[46] M. Kishimoto, T. Sueyoshi, J. Hirata, M. Amemiya, F. Hayama, *Journal of Applied Physics* **1979**, *50*, 450.
[47] T. Okada, H. Sekizawa, F. Ambe, S. Ambe, T. Yamadaya, *Journal of Magnetism and Magnetic Materials* **1983**, *31–34*, 903.
[48] A. E. Berkowitz, F. E. Parker, E. L. Hall, G. Podolsky, *IEEE Transactions on Magnetics* **1988**, *24*, 2871.
[49] Q. A. Pankhurst, R. J. Pollard, *Phys. Rev. Lett.* **1991**, *67*, 248.
[50] F. T. Parker, A. E. Berkowitz, *Phys. Rev. B* **1991**, *44*, 7437.

[51] G. Salazar-Alvarez, J. Sort, A. Uheida, M. Muhammed, S. Suriñach, M. D. Baró, J. Nogués, *J. Mater. Chem.* **2007**, *17*, 322.
[52] C. Vichery, I. Maurin, O. Proux, I. Kieffer, J.-L. Hazemann, R. Cortès, J.-P. Boilot, T. Gacoin, *J. Phys. Chem. C* **2013**, *117*, 19672.
[53] Y. Prado, N. Daffé, A. Michel, T. Georgelin, N. Yaacoub, J.-M. Grenèche, F. Choueikani, E. Otero, P. Ohresser, M.-A. Arrio, C. Cartier-dit-Moulin, P. Sainctavit, B. Fleury, V. Dupuis, L. Lisnard, J. Fresnais, *Nat Commun* **2015**, *6*, 10139.
[54] Rene. Massart, *C. R. Seances Acad. Sci., Ser. C* **1980**, *291*, 1.
[55] S. Lefebure, E. Dubois, V. Cabuil, S. Neveu, R. Massart, *J. Mater. Res.* **1998**, *13*, 2975.
[56] I. J. Bruvera, P. Mendoza Zélis, M. Pilar Calatayud, G. F. Goya, F. H. Sánchez, *Journal of Applied Physics* **2015**, *118*, 184304.
[57] L. Néel, *C. R. Seances Acad. Sci.* **1949**, *228*, 664.
[58] W. F. Brown, *Phys. Rev.* **1963**, *130*, 1677.
[59] S. Gota, M. Gautier-Soyer, M. Sacchi, *Phys. Rev. B* **2000**, *62*, 4187.
[60] A. Palii, B. Tsukerblat, S. Klokishner, K. R. Dunbar, J. M. Clemente-Juan, E. Coronado, *Chem. Soc. Rev.* **2011**, *40*, 3130.
[61] E. Garlatti, T. Guidi, A. Chiesa, S. Ansbro, M. L. Baker, J. Ollivier, H. Mutka, G. A. Timco, I. Vitorica-Yrezabal, E. Pavarini, P. Santini, G. Amoretti, R. E. P. Winpenny, S. Carretta, *Chem. Sci.* **2018**, *9*, 3555.
[62] A. Scheybal, T. Ramsvik, R. Bertschinger, M. Putero, F. Nolting, T. A. Jung, *Chemical Physics Letters* **2005**, *411*, 214.
[63] H. Wende, M. Bernien, J. Luo, C. Sorg, N. Ponpandian, J. Kurde, J. Miguel, M. Piantek, X. Xu, P. Eckhold, W. Kuch, K. Baberschke, P. M. Panchmatia, B. Sanyal, P. M. Oppeneer, O. Eriksson, *Nat Mater* **2007**, *6*, 516.
[64] S. Javaid, M. Bowen, S. Boukari, L. Joly, J.-B. Beaufrand, X. Chen, Y. J. Dappe, F. Scheurer, J.-P. Kappler, J. Arabski, W. Wulfhekel, M. Alouani, E. Beaurepaire, *Phys. Rev. Lett.* **2010**, *105*, 077201.
[65] C. Wäckerlin, D. Chylarecka, A. Kleibert, K. Müller, C. Iacovita, F. Nolting, T. A. Jung, N. Ballav, *Nat. Commun.* **2010**, *1*, 61.
[66] E. Annese, J. Fujii, I. Vobornik, G. Panaccione, G. Rossi, *Phys. Rev. B* **2011**, *84*, 174443.
[67] C. Wäckerlin, K. Tarafder, D. Siewert, J. Girovsky, T. Hählen, C. Iacovita, A. Kleibert, F. Nolting, T. A. Jung, P. M. Oppeneer, N. Ballav, *Chem. Sci.* **2012**, *3*, 3154.
[68] E. Annese, F. Casolari, J. Fujii, G. Rossi, *Phys. Rev. B* **2013**, *87*, 054420.
[69] F. Djeghloul, F. Ibrahim, M. Cantoni, M. Bowen, L. Joly, S. Boukari, P. Ohresser, F. Bertran, P. Le Fèvre, P. Thakur, F. Scheurer, T. Miyamachi, R. Mattana, P. Seneor, A. Jaafar, C. Rinaldi, S. Javaid, J. Arabski, J.-P. Kappler, W. Wulfhekel, N. B. Brookes, R. Bertacco, A. Taleb-Ibrahimi, M. Alouani, E. Beaurepaire, W. Weber, *Sci Rep* **2013**, *3*, 1272.
[70] D. Klar, B. Brena, H. C. Herper, S. Bhandary, C. Weis, B. Krumme, C. Schmitz-Antoniak, B. Sanyal, O. Eriksson, H. Wende, *Phys. Rev. B* **2013**, *88*, 224424.
[71] C. Wäckerlin, P. Maldonado, L. Arnold, A. Shchyrba, J. Girovsky, J. Nowakowski, M. E. Ali, T. Hählen, M. Baljozovic, D. Siewert, A. Kleibert, K. Müllen, P. M. Oppeneer, T. A. Jung, N. Ballav, *Chem. Commun.* **2013**, *49*, 10736.
[72] A. Candini, V. Bellini, D. Klar, V. Corradini, R. Biagi, V. De Renzi, K. Kummer, N. B. Brookes, U. del Pennino, H. Wende, M. Affronte, *J. Phys. Chem. C* **2014**, *118*, 17670.
[73] J. Girovsky, K. Tarafder, C. Wäckerlin, J. Nowakowski, D. Siewert, T. Hählen, A. Wäckerlin, A. Kleibert, N. Ballav, T. A. Jung, P. M. Oppeneer, *Phys. Rev. B* **2014**, *90*, 220404.
[74] M. Gruber, F. Ibrahim, S. Boukari, H. Isshiki, L. Joly, M. Peter, M. Studniarek, V. D. Costa, H. Jabbar, V. Davesne, U. Halisdemir, J. Chen, J. Arabski, E. Otero, F. Choueikani, K. Chen, P. Ohresser, W. Wulfhekel, F. Scheurer, W. Weber, M. Alouani, E. Beaurepaire, M. Bowen, *Nature Materials* **2015**, *14*, 981.

[75] M. Gruber, F. Ibrahim, S. Boukari, L. Joly, V. Da Costa, M. Studniarek, M. Peter, H. Isshiki, H. Jabbar, V. Davesne, J. Arabski, E. Otero, F. Choueikani, K. Chen, P. Ohresser, W. Wulfhekel, F. Scheurer, E. Beaurepaire, M. Alouani, W. Weber, M. Bowen, *Nano Lett.* **2015**, *15*, 7921.

[76] M. S. Jagadeesh, A. Calloni, A. Brambilla, A. Picone, A. Lodesani, L. Duò, F. Ciccacci, M. Finazzi, G. Bussetti, *Appl. Phys. Lett.* **2019**, *115*, 082404.

[77] A. Lodi Rizzini, C. Krull, T. Balashov, A. Mugarza, C. Nistor, F. Yakhou, V. Sessi, S. Klyatskaya, M. Ruben, S. Stepanow, P. Gambardella, *Nano Lett.* **2012**, *12*, 5703.

[78] J. Klanke, E. Rentschler, K. Medjanik, D. Kutnyakhov, G. Schönhense, S. Krasnikov, I. V. Shvets, S. Schuppler, P. Nagel, M. Merz, H. J. Elmers, *Phys. Rev. Lett.* **2013**, *110*, 137202.

[79] V. E. Campbell, M. Tonelli, I. Cimatti, J.-B. Moussy, L. Tortech, Y. J. Dappe, E. Rivière, R. Guillot, S. Delprat, R. Mattana, P. Seneor, P. Ohresser, F. Choueikani, E. Otero, F. Koprowiak, V. G. Chilkuri, N. Suaud, N. Guihéry, A. Galtayries, F. Miserque, M.-A. Arrio, P. Sainctavit, T. Mallah, *Nat Commun* **2016**, *7*, 13646.

[80] B. T. Thole, P. Carra, F. Sette, G. van der Laan, *Phys. Rev. Lett.* **1992**, *68*, 1943.

[81] M. Altarelli, *Phys. Rev. B* **1993**, *47*, 597.

[82] P. Carra, B. T. Thole, M. Altarelli, X. Wang, *Phys. Rev. Lett.* **1993**, *70*, 694.

[83] C. Piamonteze, P. Miedema, F. M. F. de Groot, *Phys. Rev. B* **2009**, *80*, 184410.

[84] "Quanty - a quantum many body script language - Quanty," can be found under https://quanty.org/, **n.d.**

[85] M. W. Haverkort, M. Zwierzycki, O. K. Andersen, *Phys. Rev. B* **2012**, *85*, 165113.

[86] M. W. Haverkort, *J. Phys.: Conf. Ser.* **2016**, *712*, 012001.

[87] C. J. Davies, G. A. Solan, J. Fawcett, *Polyhedron* **2004**, *23*, 3105.

[88] P. Ohresser, E. Otero, F. Choueikani, K. Chen, S. Stanescu, F. Deschamps, T. Moreno, F. Polack, B. Lagarde, J.-P. Daguerre, F. Marteau, F. Scheurer, L. Joly, J.-P. Kappler, B. Muller, O. Bunau, P. Sainctavit, *Review of Scientific Instruments* **2014**, *85*, 013106.

[89] C. T. Chen, Y. U. Idzerda, H.-J. Lin, N. V. Smith, G. Meigs, E. Chaban, G. H. Ho, E. Pellegrin, F. Sette, *Phys. Rev. Lett.* **1995**, *75*, 152.

Supplementary Information

Room-temperature-persistent magnetic interaction between coordination complexes and nanoparticles in maghemite-based nanohybrids.

Leonardo Curti, Yoann Prado, Aude Michel, Delphine Talbot, Benoît Baptiste, Edwige Otero, Philippe Ohresser, Yves Journaux, Christophe Cartier-dit-Moulin, Vincent Dupuis, Benoit Fleury, Philippe Sainctavit, Marie-Anne Arrio,* Jérôme Fresnais* and Laurent Lisnard*

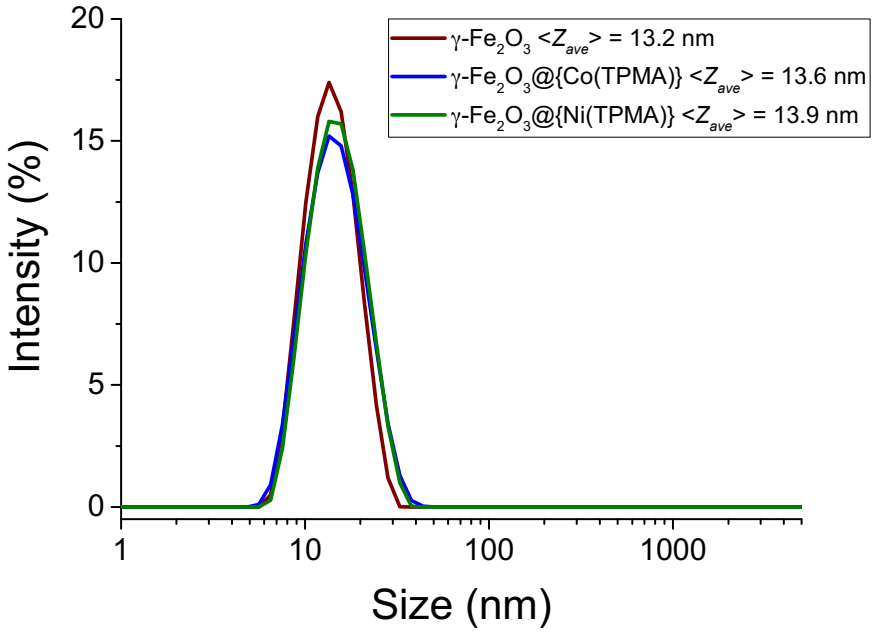

Figure S1. Intensity profiles of the DLS measurements for the as synthesized H_2O:MeOH 1:1 solutions of **γ-Fe_2O_3**, **γ-Fe_2O_3@{Co(TPMA)}** and **γ-Fe_2O_3@{Ni(TPMA)}** at 25°C.

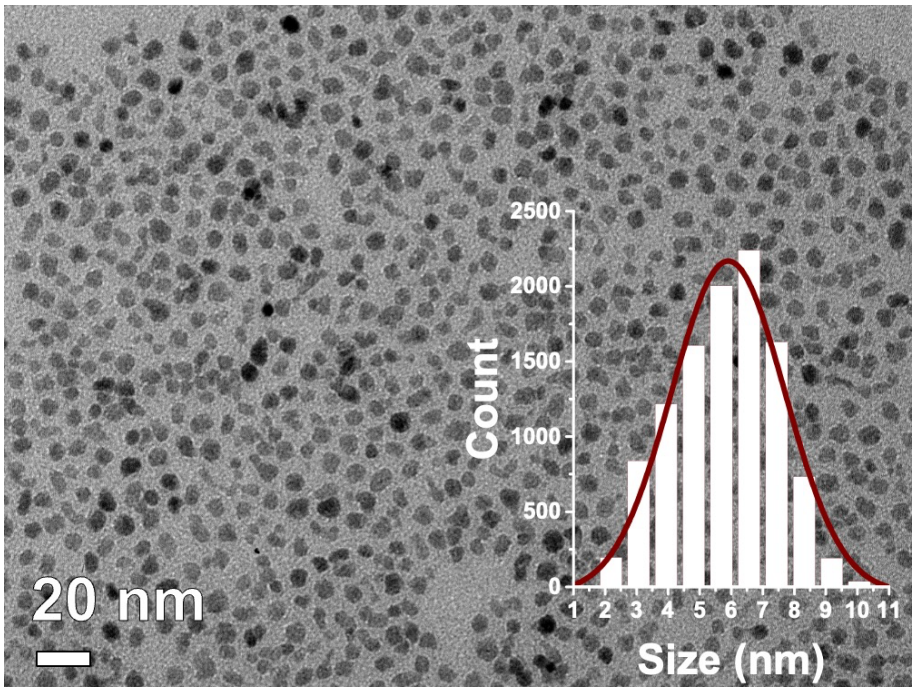

Figure S2. TEM image and distribution profile of the **γ-Fe_2O_3** nanoparticles (5.90 ± 1.8 nm).

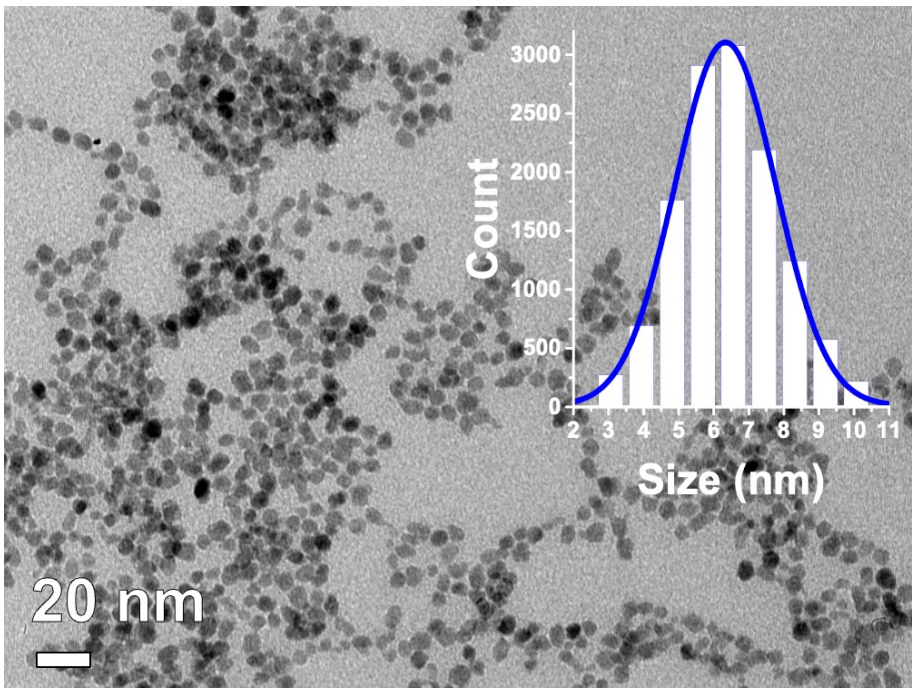

Figure S3. TEM image and distribution profile of the γ-Fe_2O_3 nanoparticles functionalized with [Co(TPMA)Cl_2], **γ-Fe_2O_3@{Co(TPMA)}** (6.33 ± 1.4 nm).

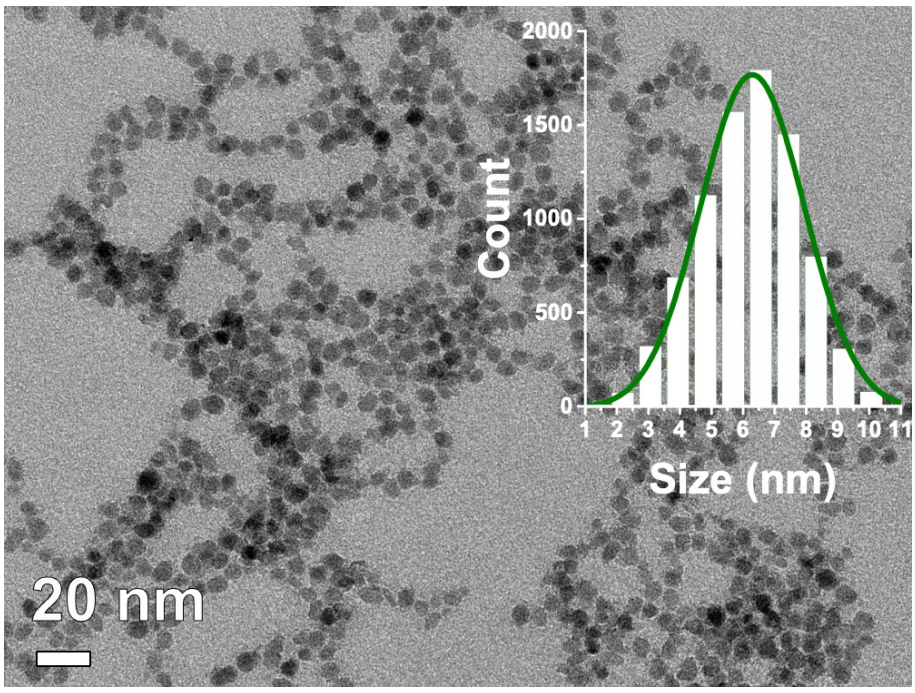

Figure S4. TEM image and distribution profile of the γ-Fe_2O_3 nanoparticles functionalized with [Ni(TPMA)Cl_2], **γ-Fe_2O_3@{Ni(TPMA)}** (6.33 ± 1.6 nm);

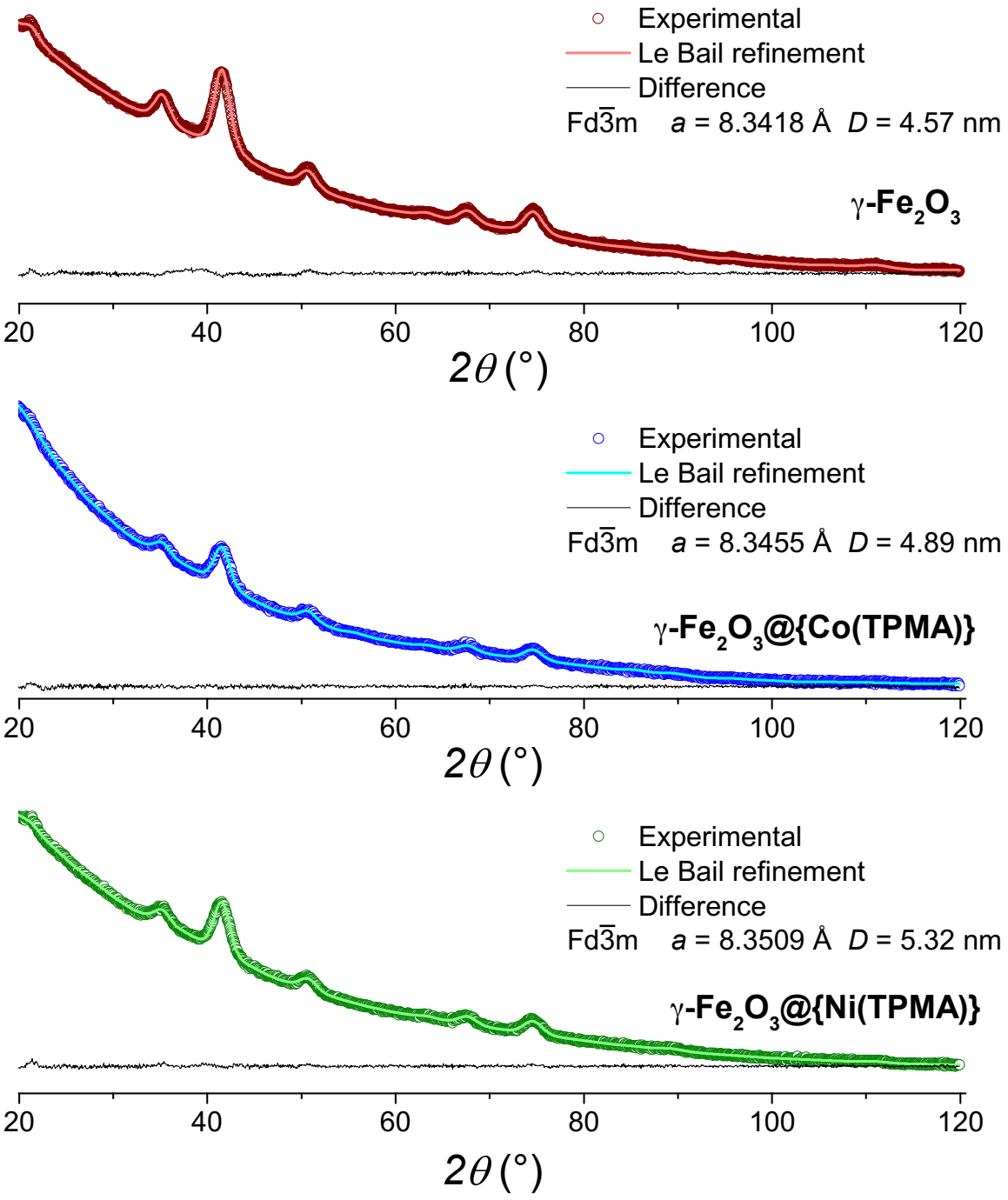

Figure S5. Powder X-ray diffraction patterns, Le Bail fit results and size determinations for compounds γ-Fe_2O_3, γ-Fe_2O_3@{Co(TPMA)} and γ-Fe_2O_3@{Ni(TPMA)}.

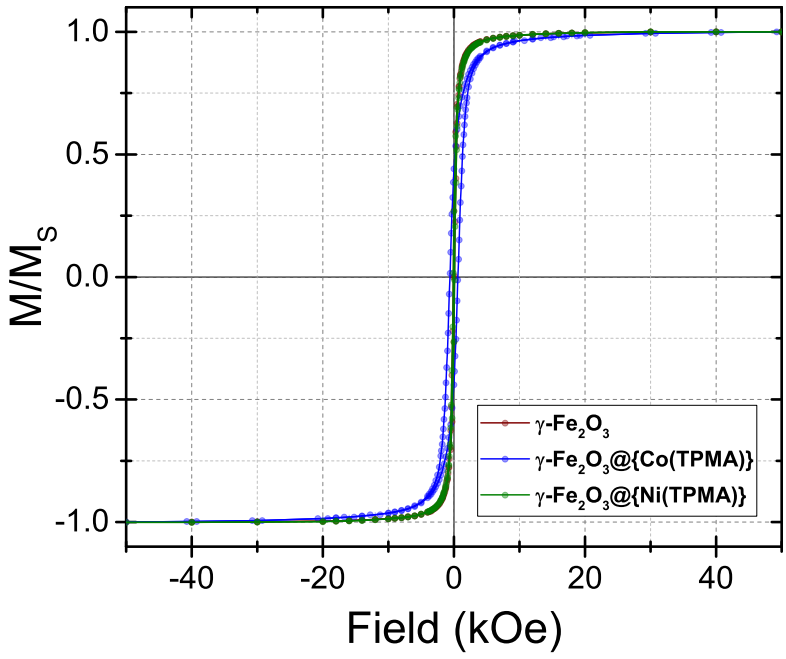

Figure S6. Field-dependence of the normalized magnetization for **γ-Fe_2O_3**, **γ-Fe_2O_3@{Co(TPMA)}** and **γ-Fe_2O_3@{Ni(TPMA)}** measured by SQUID at 5 K and in the ± 50 kOe range.

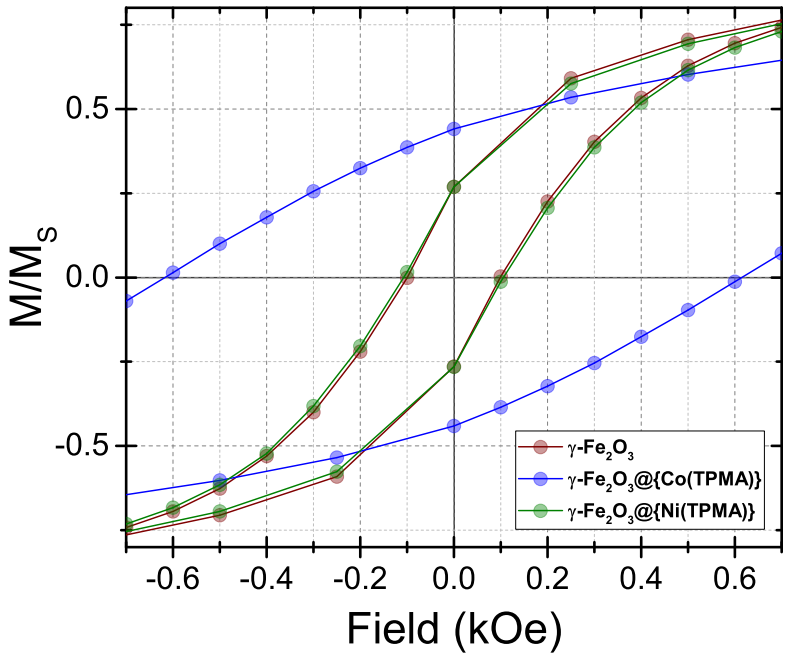

Figure S7. ± 700 Oe region of the field-dependence of the normalized magnetization for **γ-Fe_2O_3**, **γ-Fe_2O_3@{Co(TPMA)}** and **γ-Fe_2O_3@{Ni(TPMA)}** measured by SQUID at 5 K and in the ± 50 kOe range.

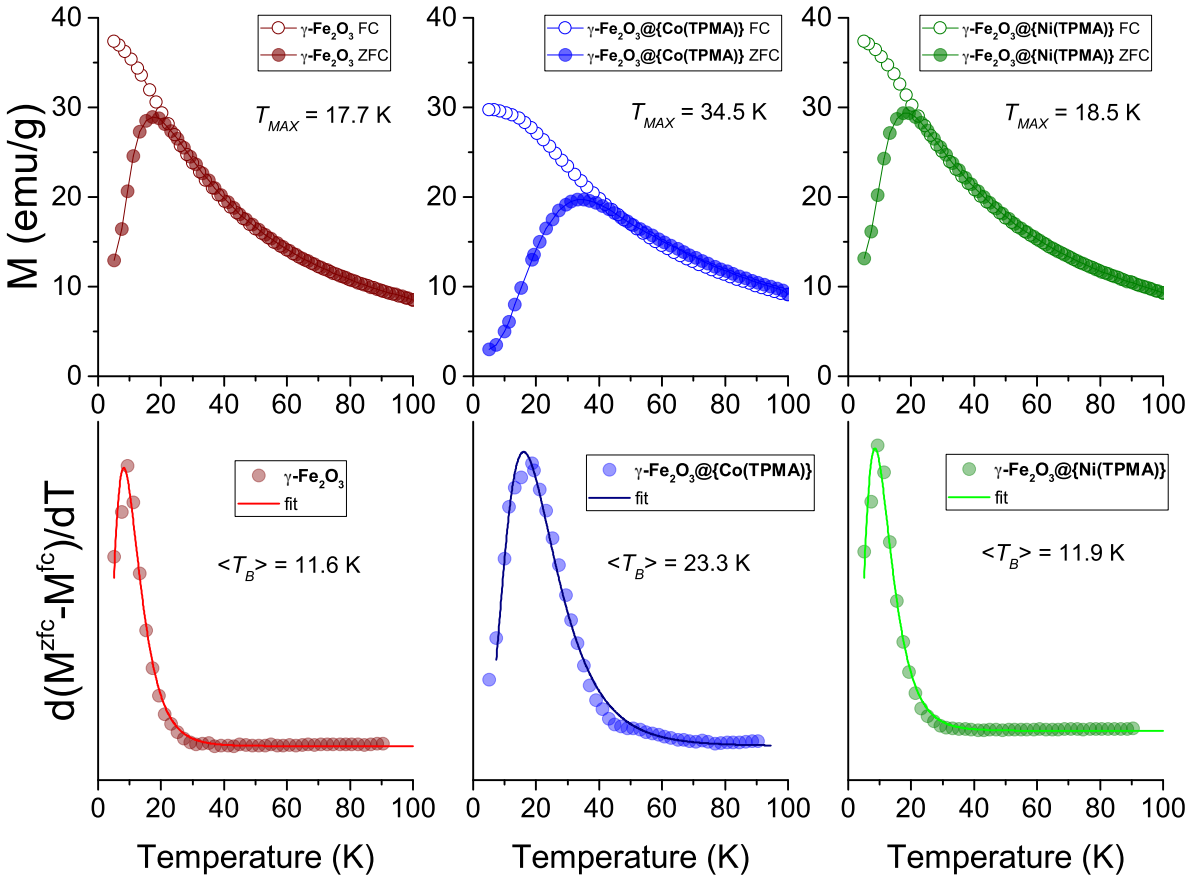

Figure S8. ZFC/FC curves measured by SQUID at 50 Oe between 5 and 100 K, with T_{MAX} values and fitting of $\langle T_B \rangle$ values for compounds **γ-Fe_2O_3**, **γ-Fe_2O_3@{Co(TPMA)}** and **γ-Fe_2O_3@{Ni(TPMA)}**.

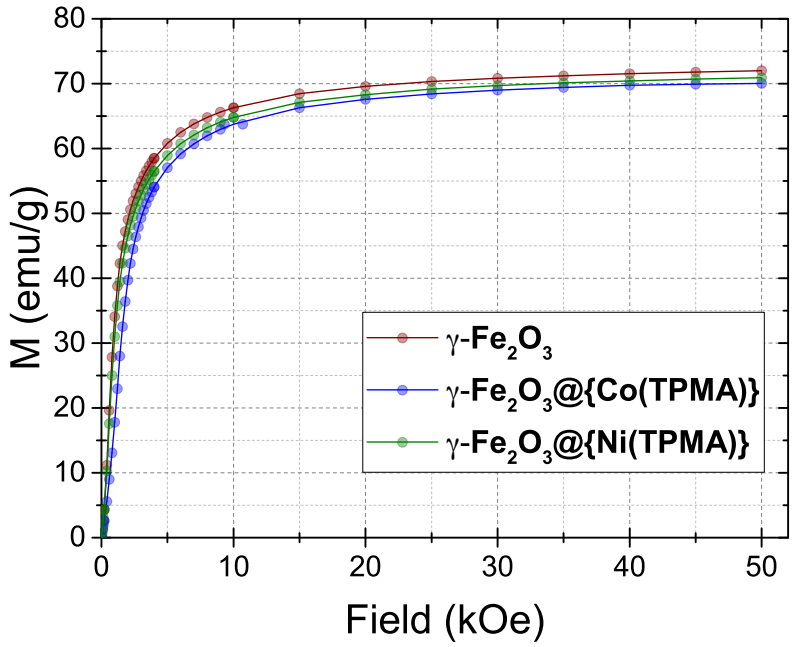

Figure S9. 1st magnetization curves measured by SQUID at 5 K from 0 to 50 kOe for **γ-Fe_2O_3**, **γ-Fe_2O_3@{Co(TPMA)}** and **γ-Fe_2O_3@{Ni(TPMA)}**.

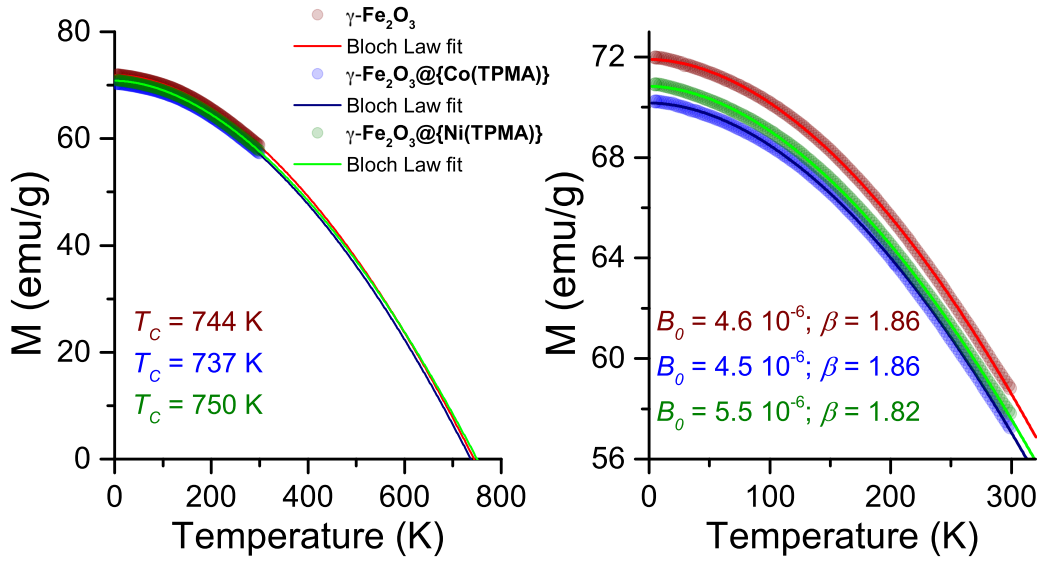

Figure S10. Temperature-dependence of the saturation magnetization measured by SQUID between 5 and 300 K at 50 kOe, with $M_S(T) = M_S(0)[1-B_0T^{\beta}]$ Bloch Law fit parameters and T_C determination for compounds **γ-Fe₂O₃**, **γ-Fe₂O₃@{Co(TPMA)}** and **γ-Fe₂O₃@{Ni(TPMA)}**.

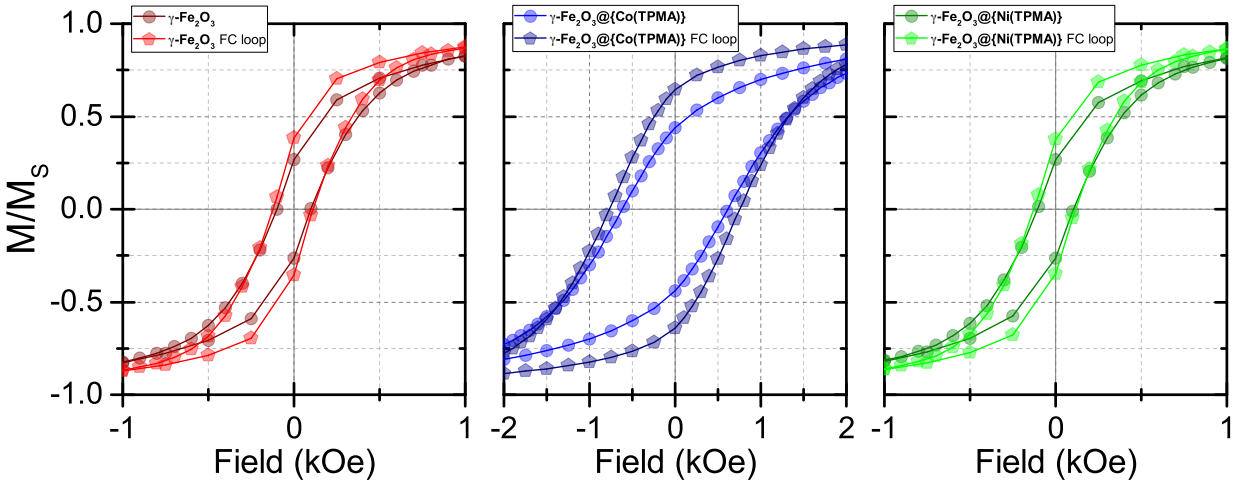

Figure S11. Hysteresis loops for **γ-Fe₂O₃**, **γ-Fe₂O₃@{Co(TPMA)}** and **γ-Fe₂O₃@{Ni(TPMA)}** measured by SQUID at 5 K and in the ± 50 kOe range and after a FC procedure at 50 kOe from 250 to 5 K.

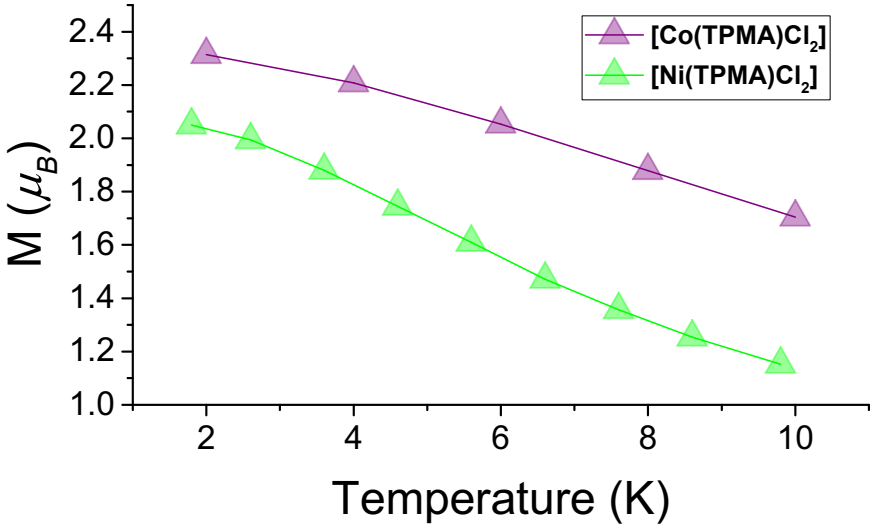

Figure S12. Low temperature magnetization curves for **[Co(TPMA)Cl$_2$]** and **[Ni(TPMA)Cl$_2$]** measured by SQUID at 60 kOe.

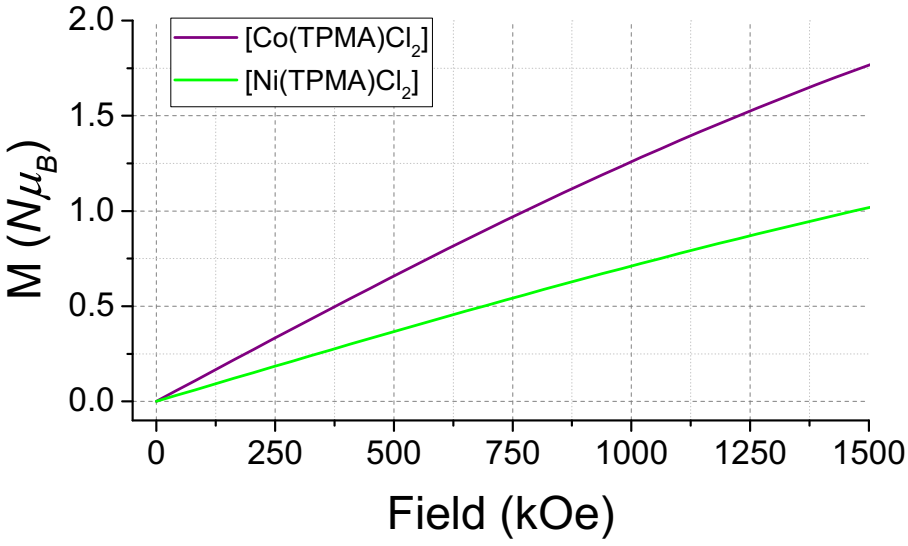

Figure S13. Room temperature simulated magnetization curves for the complexes **[Co(TPMA)Cl$_2$]** and **[Ni(TPMA)Cl$_2$]**, using PHI.[1] The parameters used for the simulation of the M *v.* H curves have been determined fitting the magnetic data for the complexes. 2500 Oe DC magnetic susceptibility and 2-10 K magnetization curves were measured for each complex. Polycrystalline samples of the latter were constrained in pressed parafilm and placed in gel capsule. Data were corrected for the sample holder and sample diamagnetic contributions. Using PHI[1], the best simultaneous fit of all data for each complex gave the parameters used above and are the following: g_{iso} = 2.06, λ = -96 cm^{-1}, α = 1.35, Δ = 521 cm^{-1}, for **[Co(TPMA)Cl$_2$]**; g_{iso} = 2.22, D = -5.1 cm^{-1}, E = 0.3 cm^{-1} for **[Ni(TPMA)Cl$_2$]**.

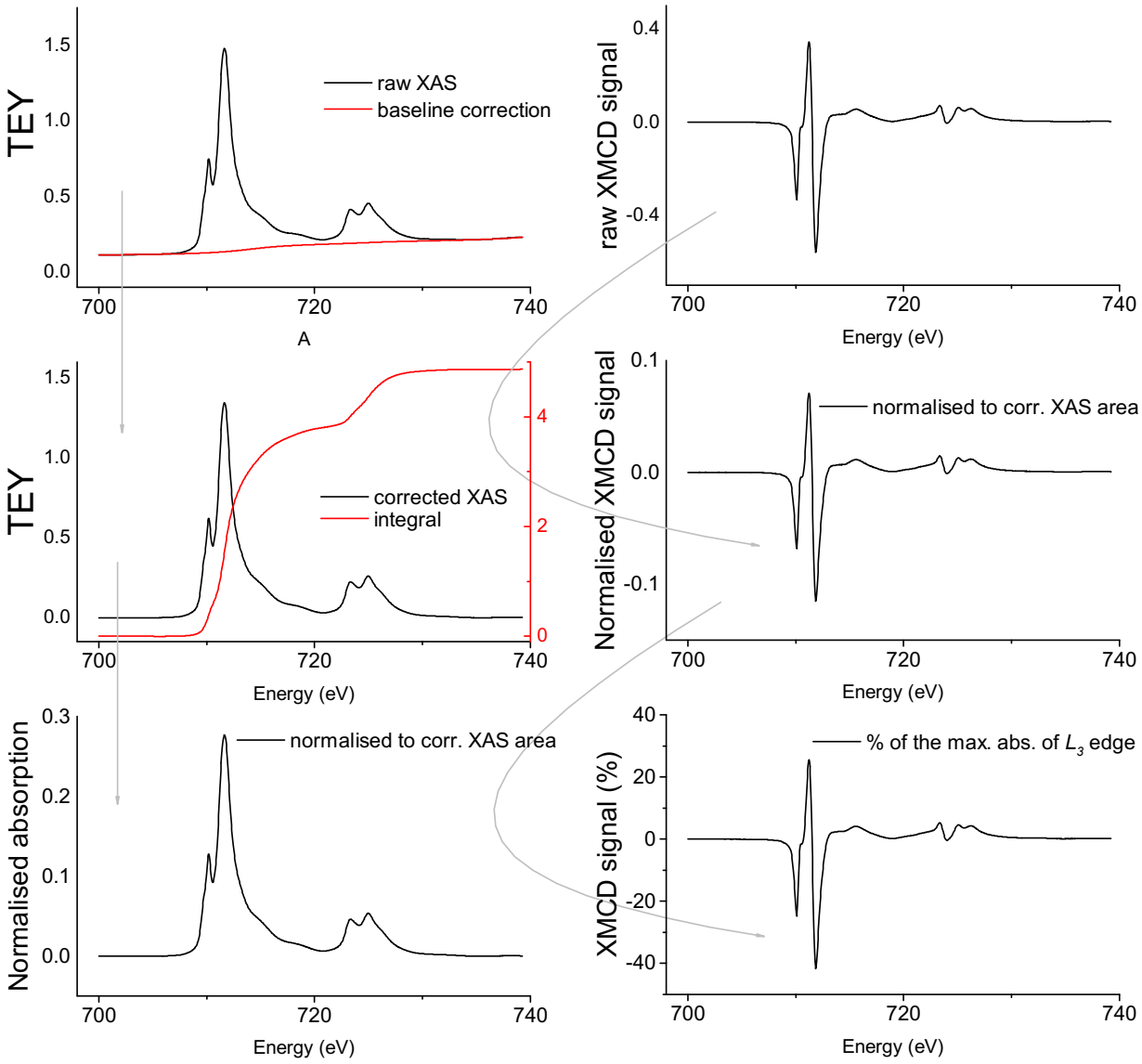

Figure S14. Graphical representation of the different steps for the normalization of the Fe $L_{2,3}$ edges XAS spectra and XMCD signals in **γ-Fe_2O_3**, **γ-Fe_2O_3@{Co(TPMA)}** and **γ-Fe_2O_3@{Ni(TPMA)}**.

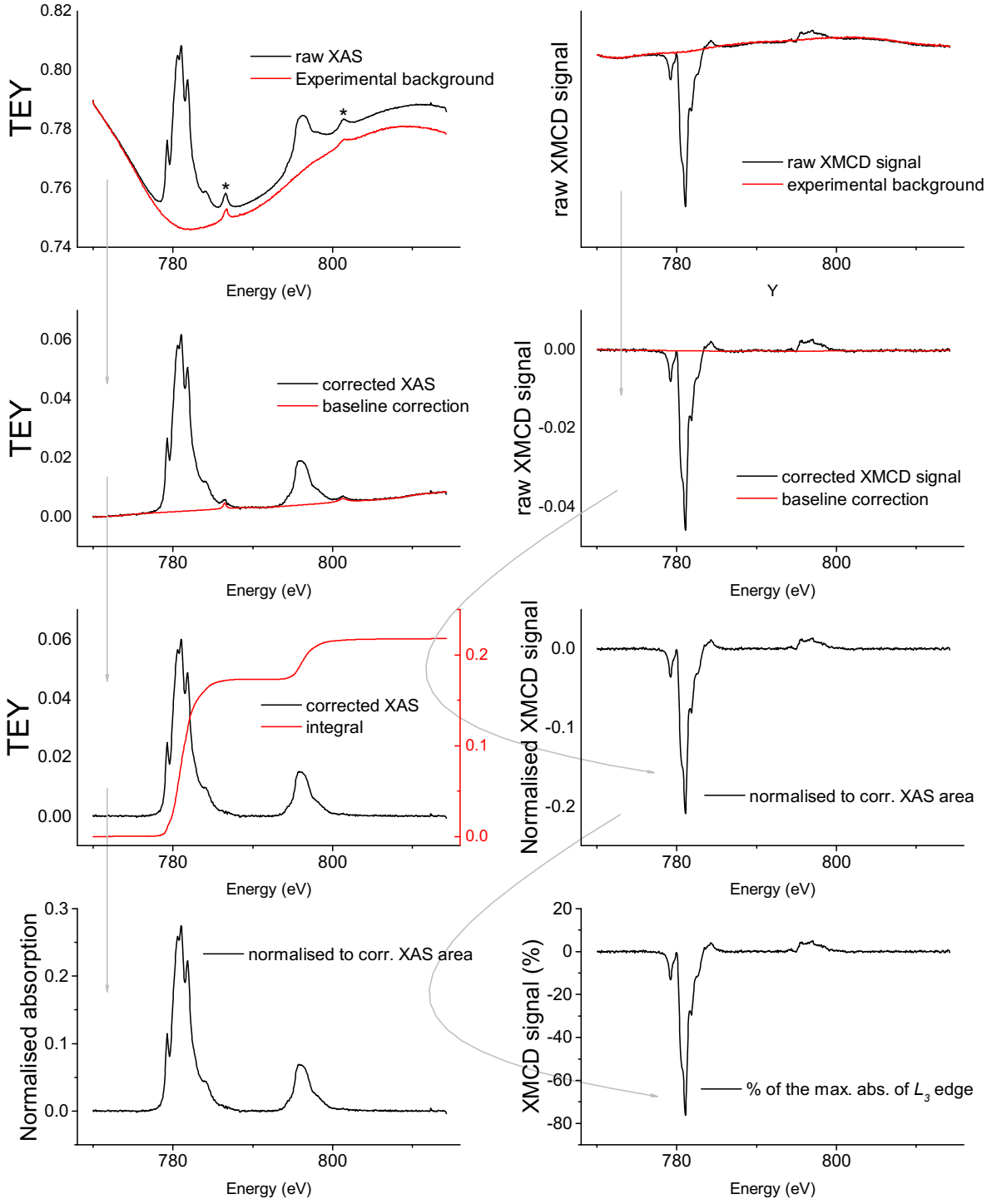

Figure S15. Graphical representation of the different steps for the normalization of the Co $L_{2,3}$ edges XAS spectra and XMCD signals in **γ-Fe_2O_3@{Co(TPMA)}**. The same method was used for **γ-Fe_2O_3@{Ni(TPMA)}**. Asterisks indicate the $M_{4,5}$ edges absorption peaks coming from trace amounts of Ba in the Si wafer.

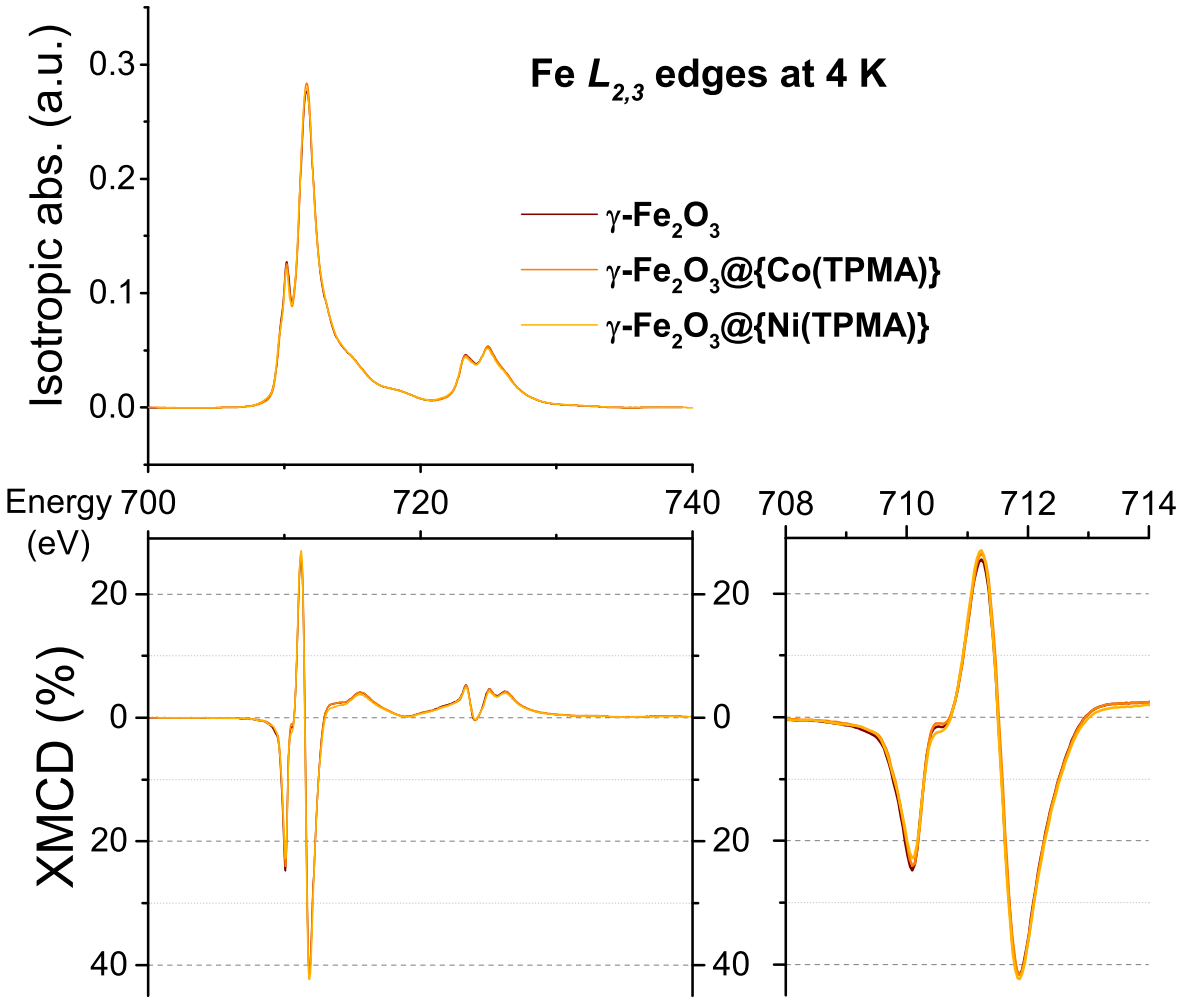

Figure S16. Comparison of the Fe $L_{2,3}$ edges measured at 4 K and ± 60 kOe in **γ-Fe_2O_3**, **γ-Fe_2O_3@{Co(TPMA)}** and **γ-Fe_2O_3@{Ni(TPMA)}**.

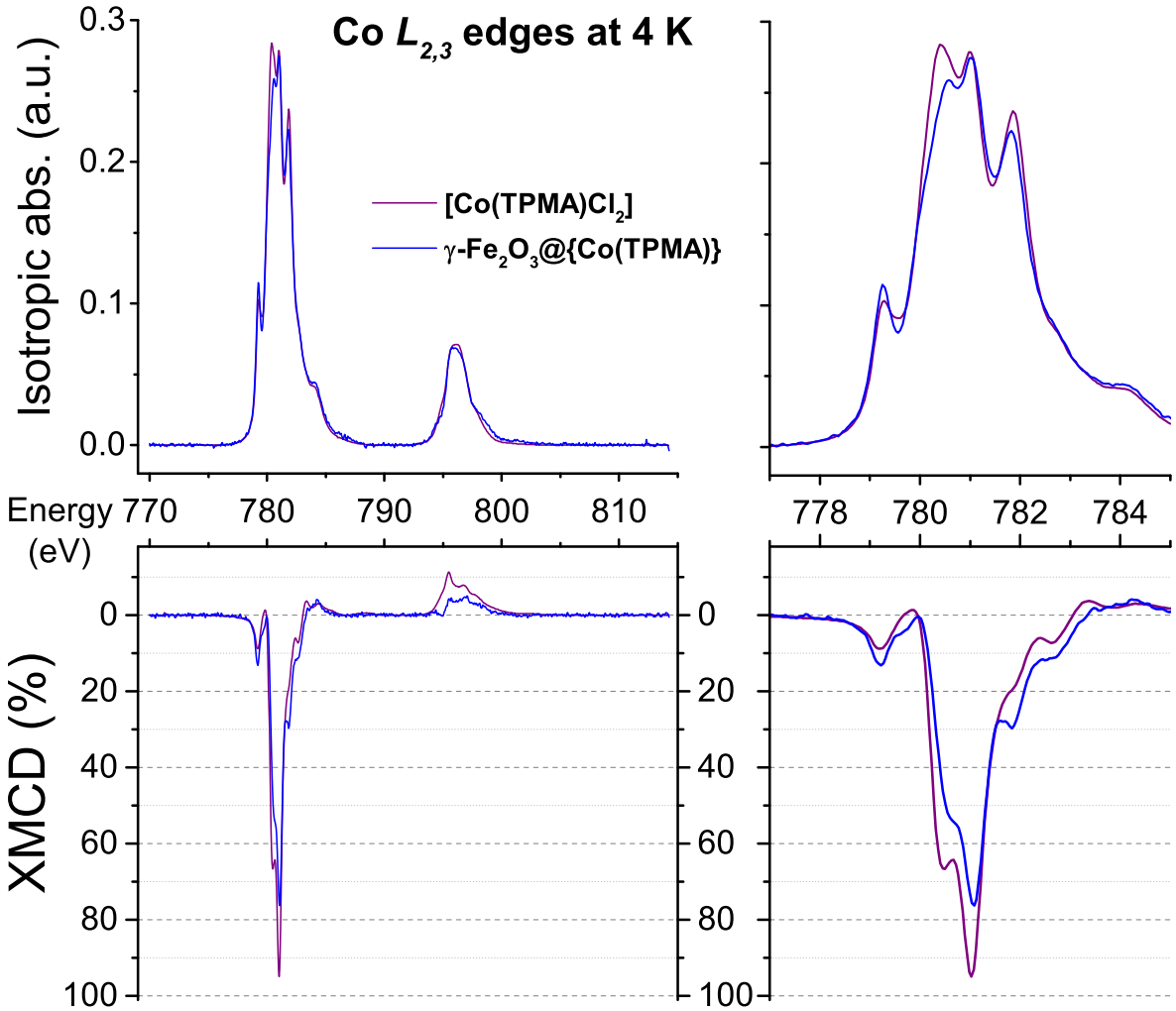

Figure S17. Comparison of the Co $L_{2,3}$ edges measured at 4 K and ± 60 kOe in γ-Fe_2O_3@{Co(TPMA)} and [Co(TPAM)Cl_2].

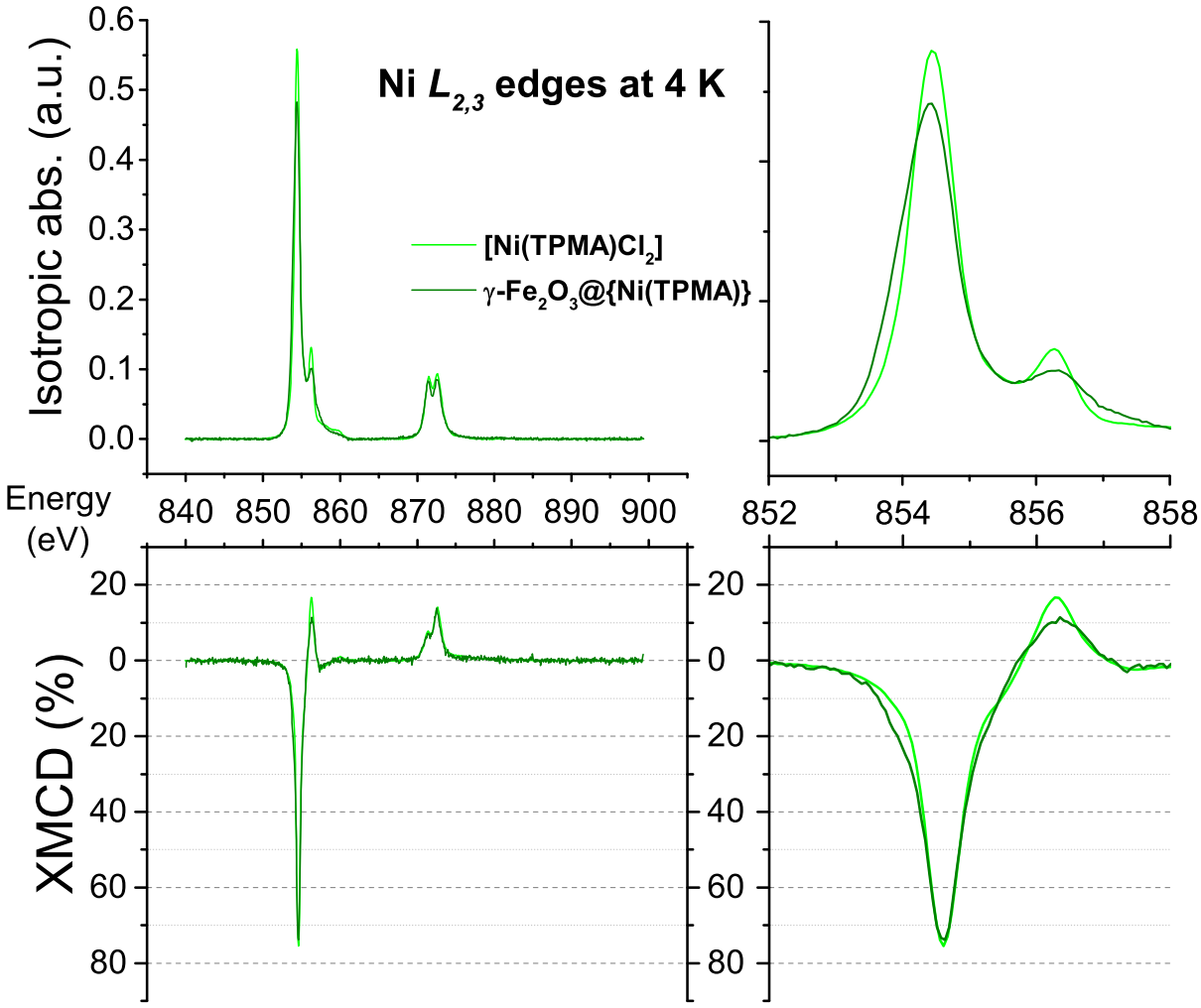

Figure S18. Comparison of the Ni $L_{2,3}$ edges measured at 4 K and ± 60 kOe in γ-Fe_2O_3@{Ni(TPMA)} and [Ni(TPAM)Cl_2].

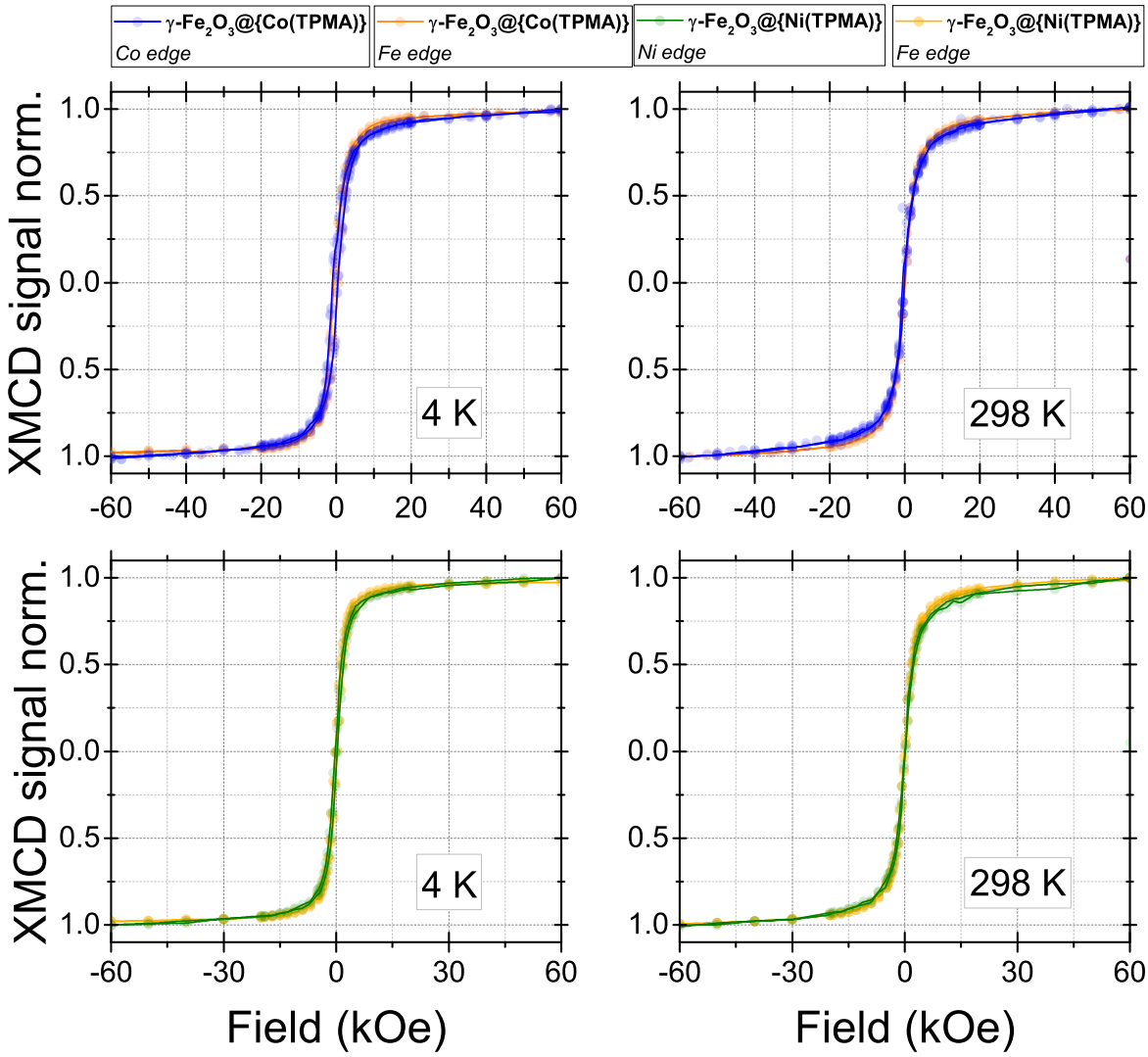

Figure S19. Field-dependence of the *Oh* Fe L_3, Co L_3 and Ni L_3 edges normalized XMCD signals for **γ-Fe_2O_3@{Co(TPMA)}** and **γ-Fe_2O_3@{Ni(TPMA)}** at 4 K and 298 K.

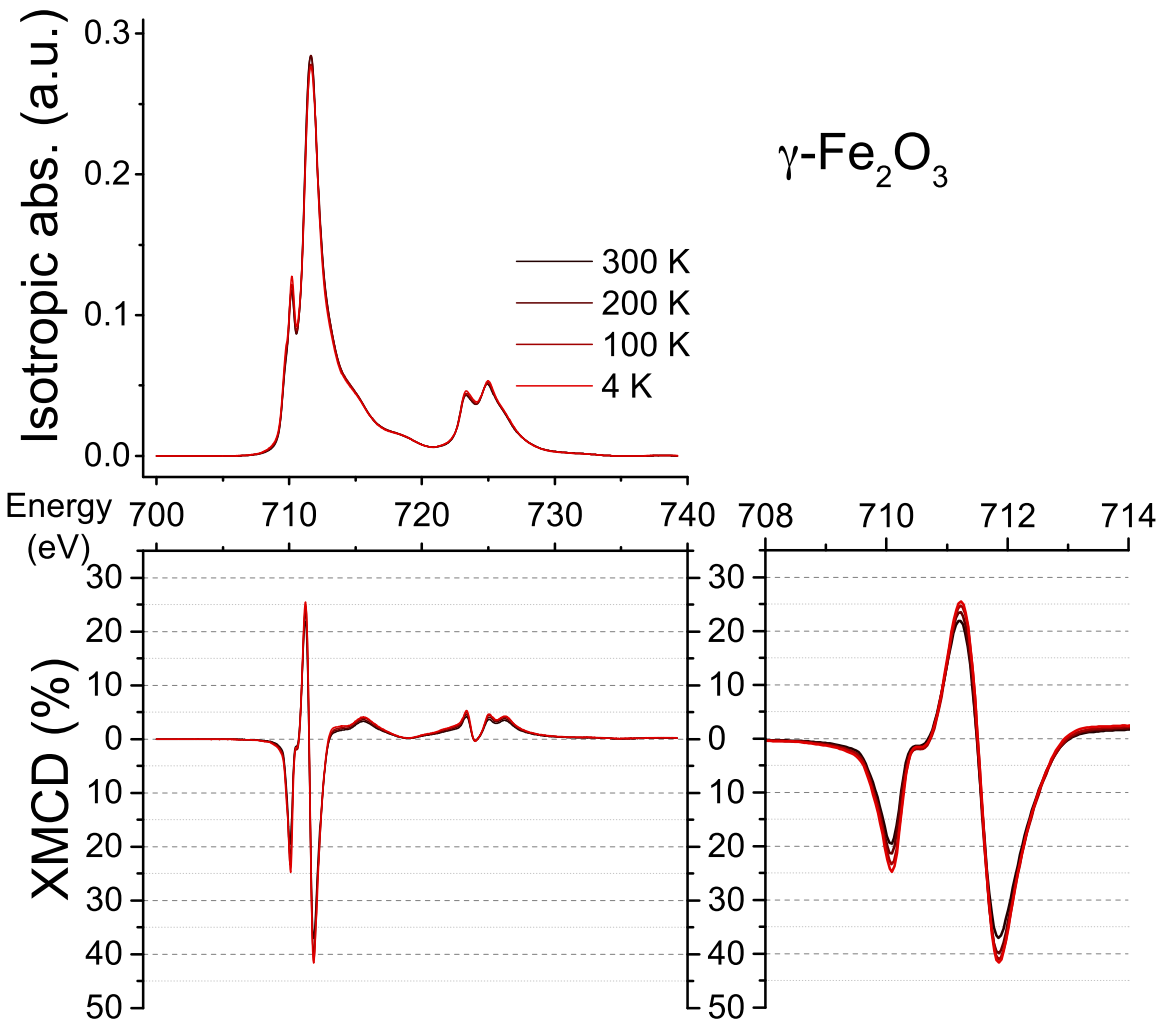

Figure S20. Temperature-dependence of the XAS spectra and XMCD signals in **γ-Fe_2O_3**, from 5 to 300 K at ± 60 kOe.

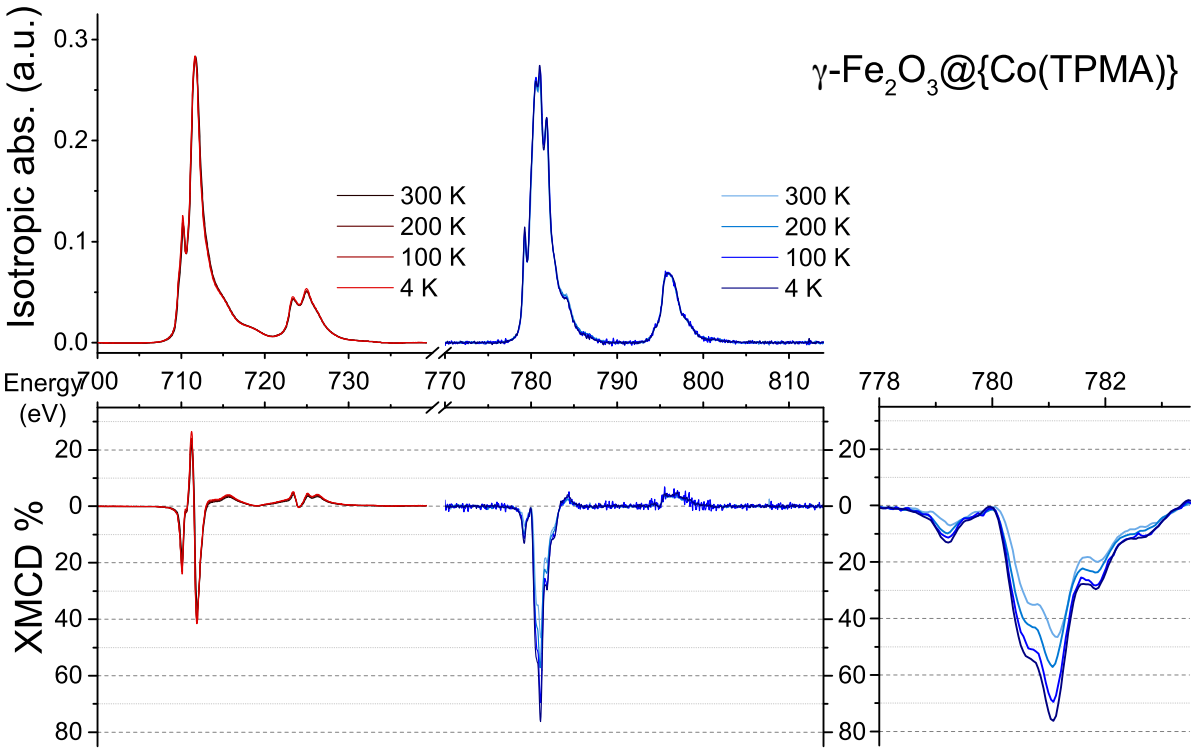

Figure S21. Temperature-dependence of the XAS spectra and XMCD signals in **γ-Fe_2O_3@{Co(TPMA)}**, from 5 to 300 K at ± 60 kOe.

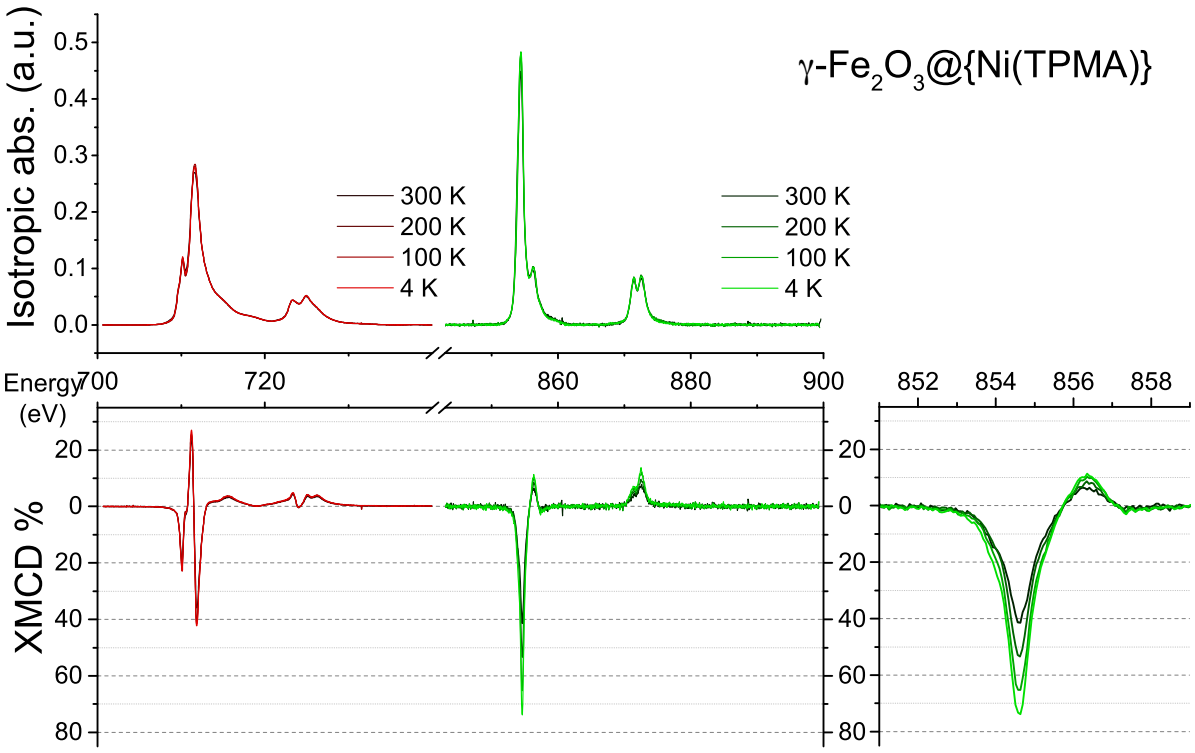

Figure S22. Temperature-dependence of the XAS spectra and XMCD signals in **γ-Fe_2O_3@{Ni(TPMA)}**, from 5 to 300 K at ± 60 kOe.

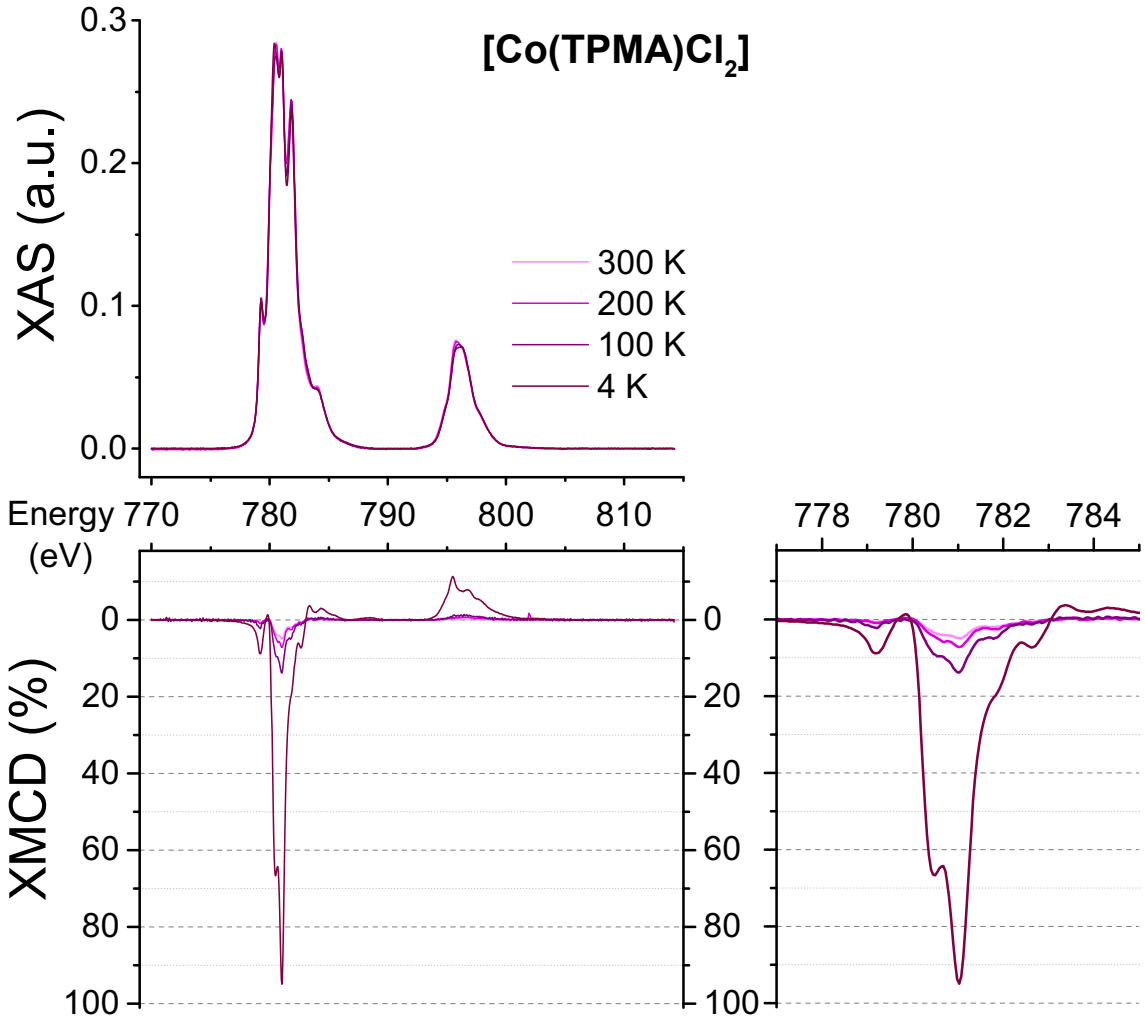

Figure S23. Temperature-dependence of the XAS spectra and XMCD signals in **[Co(TPAM)Cl$_2$]**, from 5 to 300 K at ± 60 kOe.

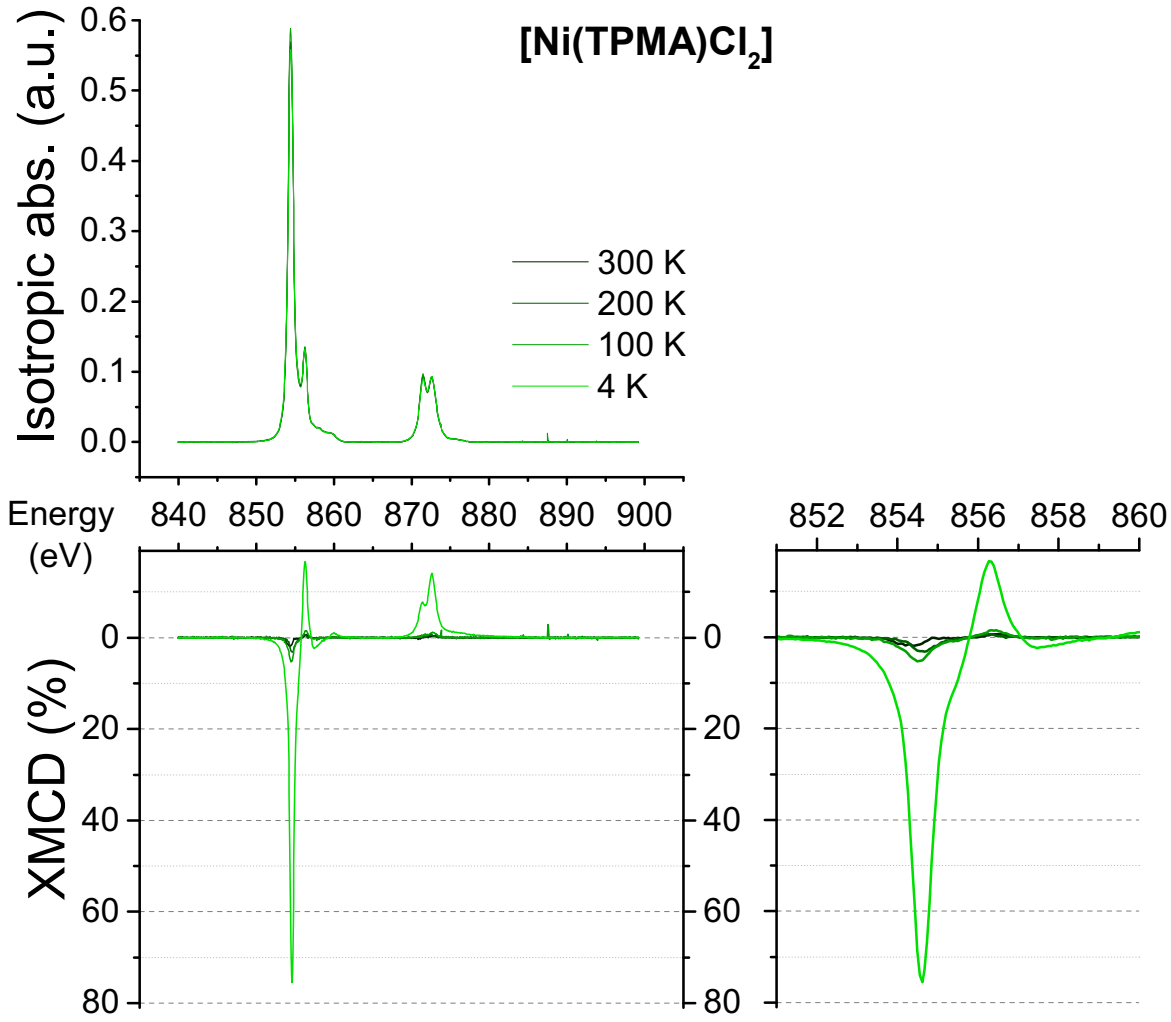

Figure S24. Temperature-dependence of the XAS spectra and XMCD signals in **[Ni(TPAM)Cl_2]**, from 5 to 300 K at ± 60 kOe.

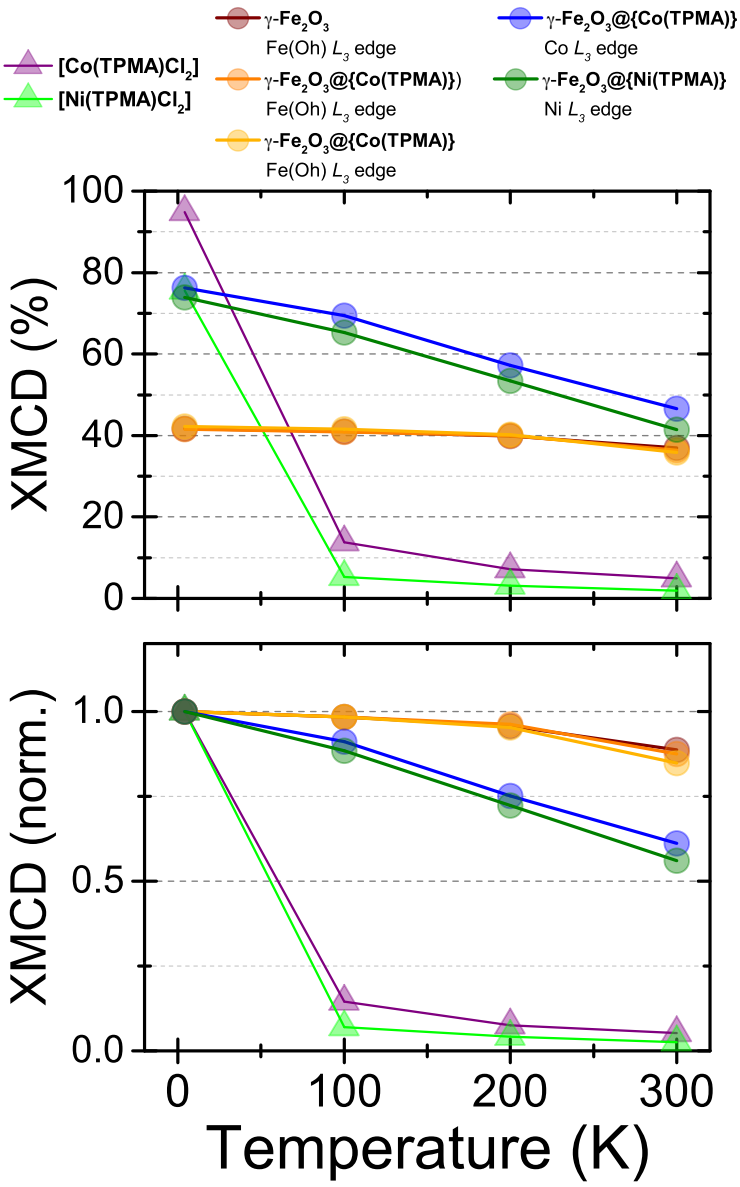

Figure S25. Temperature-dependence of the intensity of the XMCD signals (in % of the XAS maxima at the top, normalized to 1 at the bottom) at the *Oh* Fe(III), Co and Ni L_3 edge for **γ-Fe_2O_3**, **γ-Fe_2O_3@{Co(TPMA)}**, **γ-Fe_2O_3@{Ni(TPMA)}**, **[Co(TPMA)Cl_2]** and **[Ni(TPMA)Cl_2]**,

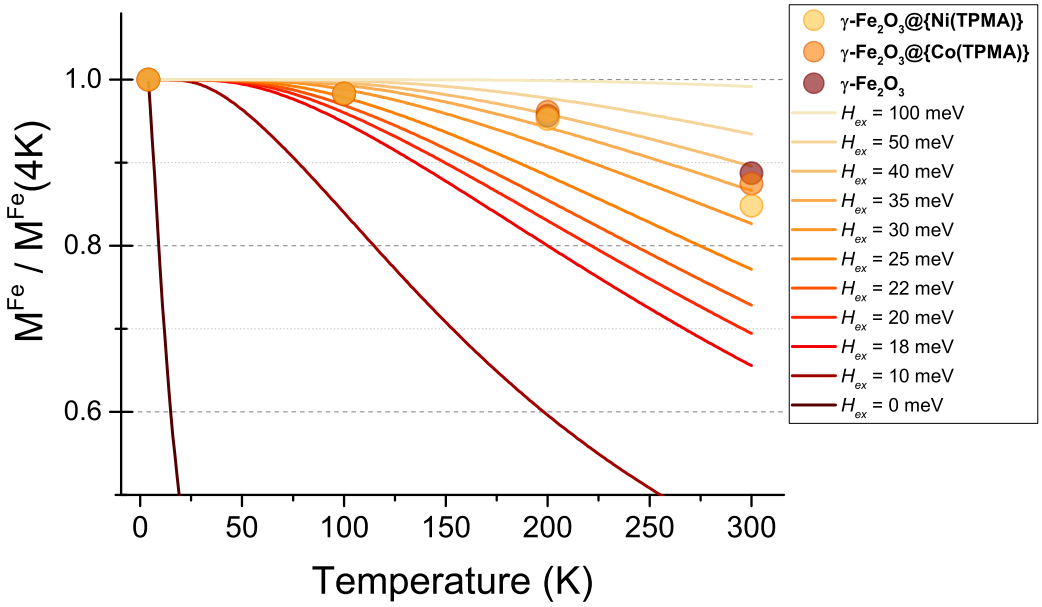

Figure S26. Simulation of *M(T)/M(4K)* for different exchange field values together with the normalized experimental *Oh* Fe(III) XMCD values for **γ-Fe_2O_3**, **γ-Fe_2O_3@{Co(TPMA)}**, and **γ-Fe_2O_3@{Ni(TPMA)}**. The magnetic moments were calculated within the Ligand Field Multiplet theory with the Quanty code.[2–4] The eigenstates of Fe(II) were calculated using *Oh* symmetry and a fixed H_{ex} value, within an external 60 kOe magnetic field. A ligand field strength of 10*Dq* = 1 eV was used. The magnetic moments were calculated at each temperature using the Boltzmann distribution.

Estimation of the number of iron(III) ions (n) influenced by the Co(II) complexes:

$$n_{Fe}^{tot} = 4908$$

γ-Fe_2O_3 : 1

γ-Fe_2O_3@{Co(TPMA)} : 2

$$H_{C_{Fe}}^{\mathbf{1}} = 270\ Oe;\ H_{C_{Fe}}^{\mathbf{2}} = 590\ Oe; H_{C_{Co}}^{\mathbf{2}} = 710\ Oe$$

$$H_{C_{Fe}}^{\mathbf{2}} = \frac{(n_{Fe}^{tot} - n) \times H_{C_{Fe}}^{\mathbf{1}} + n \times H_{C_{Co}}^{\mathbf{2}}}{n_{Fe}^{tot}}$$

$$n = \frac{n_{Fe}^{tot} \times (H_{C_{Fe}}^{\mathbf{2}} - H_{C_{Fe}}^{\mathbf{1}})}{H_{C_{Co}}^{\mathbf{2}} - H_{C_{Fe}}^{\mathbf{1}}} = 3570$$

1N. F. Chilton, R. P. Anderson, L. D. Turner, A. Soncini and K. S. Murray, *J. Comput. Chem.*, 2013, 34, 1164–1175.

2Quanty - a quantum many body script language - Quanty, https://quanty.org/, (accessed February 8, 2024).

3M. W. Haverkort, M. Zwierzycki and O. K. Andersen, *Phys. Rev. B*, 2012, 85, 165113.

4M. W. Haverkort, *J. Phys.: Conf. Ser.*, 2016, 712, 012001.